




# Numerical Study of the Thermal Structure and Circulation in a Large and Deep Dimictic Lake Over Tibetan Plateau

Yang Wu<sup>1,2</sup>, Anning Huang<sup>1</sup> , Youyu Lu<sup>3</sup> , Lazhu<sup>4</sup>, Xianyu Yang<sup>5</sup>, Bo Qiu<sup>1</sup> , Zhiqi Zhang<sup>1</sup>, and Xindan Zhang<sup>1,2</sup>

## Key Points:

- Three-dimensional modeling of Lake Nam Co reveals the spatial-temporal variations of thermal structure and circulations
- Heat budget analysis indicates the importance of both the lake-air heat flux and lateral heat redistribution for the thermodynamics
- Lake circulation is primarily determined by the wind-driven barotropic dynamics and baroclinic process makes a secondary contribution

<sup>1</sup>CMA-NJU Joint Laboratory for Climate Prediction Studies, School of Atmospheric Sciences, Nanjing University, Nanjing, China, <sup>2</sup>State Key Laboratory of Severe Weather, Joint Center for Atmospheric Radar Research of CMA/NJU, School of Atmospheric Sciences, Nanjing University, Nanjing, China, <sup>3</sup>Fisheries and Oceans Canada, Bedford Institute of Oceanography, Dartmouth, Canada, <sup>4</sup>Key Laboratory of Tibetan Environment Changes and Land Surface Processes, Institute of Tibetan Plateau Research, Chinese Academy of Sciences, Beijing, China, <sup>5</sup>Plateau Atmosphere and Environment Key Laboratory of Sichuan Province, College of Atmospheric Sciences, Chengdu University of Information Technology, Chengdu, China

## Correspondence to:

A. Huang,  
[anhuang@nju.edu.cn](mailto:anhuang@nju.edu.cn)

## Citation:

Wu, Y., Huang, A., Lu, Y., Lazhu, Yang, X., Qiu, B., et al. (2021). Numerical study of the thermal structure and circulation in a large and deep dimictic lake over Tibetan Plateau. *Journal of Geophysical Research: Oceans*, 126, e2021JC017517. <https://doi.org/10.1029/2021JC017517>

Received 27 APR 2021

Accepted 1 OCT 2021

**Abstract** A three-dimensional (3-D) hydrodynamic model based on the Princeton Ocean Model (POM) was applied to simulate the thermal structure and circulation of Lake Nam Co (LNC), the third largest lake over the Tibetan Plateau (TP), during May–December 2013. Compared with a spatially distributed set of one-dimensional thermal diffusion lake models, POM better reproduced the observed seasonal evolution of the horizontal distribution of lake surface temperature and the vertical thermal structure. A heat budget analysis confirmed that the lateral heat exchange made significant contributions to the horizontal variability of lake temperature. The model results showed that LNC was thermally stratified in summer, had a weak inverse stratification since mid-December, and was fully turned over during late spring and autumn. During both overturning phases, the modeled “thermal bar” was developed as a result of the density-driven convection in response to the radiative heating (surface cooling) during spring (autumn). The 3-D model results showed that the monthly mean circulation featured a predominant mid-lake cyclonic gyre throughout the ice-free period; upwelling along the western coast and strong coastal currents occurred in all months except in July–August. Model sensitivity experiments confirmed that the lake circulation was primarily driven by the barotropic dynamics of the prevailing southwesterly wind, while the baroclinic process made a secondary contribution. The results pointed out the necessity to resolve lateral processes when modeling large TP lakes.

**Plain Language Summary** The Tibetan Plateau has the highest alpine lake concentration in the world and Lake Nam Co is the third largest lake in the region. This study showed that a three-dimensional (3-D) hydrodynamic model performed better than a spatially distributed set of one-dimensional thermal diffusion lake models in reproducing the observed spatial and temporal variations of the lake temperature, and depicted the existence of lake gyre circulation, coastal currents, and upwelling. Model sensitivity experiments revealed that the lake circulation during the ice-free season was primarily driven by the prevailing southwesterly wind, while the thermal structure made a secondary contribution. The improved simulation of the thermal structure and circulation with 3-D models is important to understand the variations of the ecosystem in large lakes and the impacts of lakes on the regional weather and climate.

## 1. Introduction

Lake-air interaction plays important roles in the water and energy balances of the hydroclimatic systems at multiscale (Sharma et al., 2018), especially over the lake-rich regions such as the Tibetan Plateau (TP), which has the highest alpine lake concentration in the world (Zhang, 2018). The total number and surface area of the lake clusters distributed across TP exceed 1,200 and 47,000 km<sup>2</sup>, respectively (Ma et al., 2011; C. Q. Song et al., 2014). The presence of such a large amount of endorheic lakes exerts significant impacts on the regional weather and climate through influencing the lake-air turbulent fluxes and the atmospheric boundary structure (Biermann et al., 2014). Additionally, most TP lakes are undergoing rapid expansion

(Guo et al., 2019; G. Q. Zhang et al., 2014, 2017), which is closely associated with the glacier retreat, permafrost degradation, and evaporation/rainfall variations under the background of the pronounced climate warming over TP (X. J. Wang et al., 2017).

A number of studies on TP lakes are based on field measurements and satellite observations. For example, based on 2-year in situ water temperature records, J. B. Wang et al. (2019) demonstrated that Lake Nam Co (LNC), the third largest lake over TP, is a typical dimictic lake showing different evolution of thermal stratification between its main basin and the smaller eastern basin. The spatial variation in the stratification structure is related to the distribution of heat influenced by the lake morphometry (i.e., basin size and lake depth) and water transparency. Analogous summer thermocline developments have also been observed in many other high-altitude dimictic or meromictic TP lakes, for example, Lake Puma Yum Co (Murakami et al., 2007), Lake Tangra Yum Co (J. B. Wang et al., 2010), Lake Bangong Co, and Lake Dagze Co (M. D. Wang et al., 2014).

Due to the temporal discontinuity and spatial scarcity of the observational data, numerical models have also been adopted to study the TP lakes. Up to now, the reported models of TP lake thermodynamics all belong to the category of one-dimensional (1-D) models. These 1-D lake models adopt varying levels of simplifications for lake processes and only resolve the vertical thermal transfer related to the local surface heat flux, winds, and convective instability (Gu et al., 2015). During recent years, considerable work has been conducted to calibrate the key parameters in 1-D models, including the water/ice albedo, light attenuation coefficient, surface roughness length, and vertical mixing parameterization, and so on (Y. J. Dai et al., 2018; A. N. Huang et al., 2019; Wen et al., 2016; C. L. Xiao et al., 2016; Xu et al., 2016). However, the 1-D models exhibit disadvantages in simulating the thermodynamics of large deep lakes where three-dimensional (3-D) hydrodynamics play important roles (Bennington et al., 2014; Martynov et al., 2010; Stepanenko et al., 2014; Xue et al., 2016).

Important 3-D lake hydrodynamic processes include the thermally driven circulation, wind-induced horizontal currents, up-welling and down-welling, surface waves, internal waves, seiches, and horizontal and vertical mixing processes (e.g., Aijaz et al., 2017; Bennington et al., 2010; Gill, 1982; A. N. Huang et al., 2010; Mortimer, 1987). In many large temperate lakes, the thermal and flow states in spring and autumn are strongly affected by the presence of “thermal bar” (hereafter TB) (Boyce et al., 1989; Rao et al., 2004; Thikhomirov, 1963). TB is a narrow water zone that has a temperature of maximal water density ( $T_{dmax}$ ), features convergent descending motions, and serves as a barrier in separating the warm stratified and cold well-mixed waters (Blokhuja & Selin, 2019; Tsydenov, 2019). The thermal contrast across the TB creates a horizontal pressure (density) gradient and associated circulation. In small lakes, the thermally driven circulation directs across the TB hence sustains the heat transport from warm to cold areas (Holland & Kay, 2003; Malm, 1995; Malm et al., 1993). In large lakes where the influence of Earth’s rotation becomes significant, gyre circulations astride the TB are formed and do not make significant contribution to the heat transfer across the TB (Rao & Schwab, 2007). Wind-driven circulation and horizontal mixing are important processes for heat transfer. The advantages of 3-D over 1-D lake models were demonstrated by the inter-comparison of lake-air coupled simulations for Lake Victoria in Africa. The inter-comparison results showed that excluding the flow-dependent heat transport from warm to cold regions led to degraded simulations in the surface water temperature as well as the winds and rainfall over and downstream the lake areas (Y. Song et al., 2004).

There are 13 lakes with an individual surface area exceeding 500 km<sup>2</sup> over TP. Among them, the three largest lakes are all saltwater lakes and each has an area exceeding 2,000 km<sup>2</sup> (Lu et al., 2019). Specifically, the surface area and salinity are 4,400 km<sup>2</sup> and 12.3 g/L for Qinghai Lake; 2,349 km<sup>2</sup> and 18.7 g/L for Lake Selin Co, and 2,028 km<sup>2</sup> and 1.7 g/L for LNC. According to high-resolution remote sensing observations, these large TP lakes with complex bathymetry show significant spatiotemporal variabilities in lake surface temperature (LST) (Ke & Song, 2014; K. S. Song et al., 2016; F. Xiao et al., 2013). Compared to the deep central regions, the shallow coastal areas warm up faster in spring, and cool down rapidly in autumn, generating the persistent onshore-offshore temperature gradients. During fall-winter, the over-lake air column is commonly unstable (due to cold air over warm water), surface winds are enhanced, and can induce stronger lake circulation and flow-dependent heat transfer. In this study, for the first time, we apply the 3-D Princeton Ocean Model (POM) to simulate the lake circulation and

thermal structure in LNC, because of the availability of year-long continuous in situ observations of water temperature for model evaluation. The performance of the 3-D lake model will be compared with that of the 1-D lake component from the Weather Research and Forecast model (WRF-Lake). The 1-D model has been extensively used for offline/coupled simulations of TP lakes (Y. F. Dai et al., 2018; A. N. Huang et al., 2019; Xu et al., 2018; Wu et al., 2019; Q. H. Zhang et al., 2018; Zhu et al., 2018). The 3-D model results will be analyzed to reveal the linkages among variations of the thermal structure, lake circulation, and surface forcing. Main findings of this study will provide insights on the potential benefits of coupling 3-D lake models with atmospheric models to improve the simulation of lake-air interactions over LNC and other large TP lakes.

## 2. Material and Methods

### 2.1. Study Area and Data Sets

LNC is located at an altitude of approximately 4,730 m at the northeastern foot of the elevated Nyainqentanglha Mountains (~6,000 m altitude) in the central TP, extending from 30°30'N to 30°55'N and 90°16'E to 91°03'E (Figure 1a). It has a maximum length of about 75 km along the east-west direction, and consists of a large central basin and a small eastern basin, with the maximum depths of ~99 and ~60 m, respectively (J. B. Wang et al., 2009; J. B. Wang et al., 2019). The Nam Co basin lies in a transition region between the semiarid and semihumid zones and is mainly influenced by the southwestern monsoon and westerly systems during May–December (J. B. Wang et al., 2020).

In 2013, lake water temperature profiles, sampled at depths of 3, 6, 16, 21, 31, 36, 56, 66, and 83 m, were measured at a mooring site located in the eastern part of the central basin of LNC (purple asterisk in Figure 1b). At the same time, weather conditions were measured by an automatic weather station located approximately 1.5 km from the southeastern shoreline of LNC (red asterisk in Figure 1b). Details of the above observations are described in Lazhu et al. (2016). The observed daily lake water temperatures (derived from samples at 10 min intervals) were used for lake model initialization and validation in this study. Another data set for model validation is the Moderate Resolution Imaging Spectroradiometer (MODIS) product (MOD11A1, available at <https://modis.gsfc.nasa.gov/data/dataproduct/mod11.php>). MOD11A1 consists of both daytime and nighttime channels to provide twice-daily LST images at approximately 11:00 and 21:00 local solar time over LNC, with a spatial resolution of 1 km (Wan et al., 2004).

The automatic weather station provided observed daily surface solar radiation, surface downward longwave radiation, relative humidity at 10 m above ground, air temperature at 2 m above ground, and surface pressure and wind speed. The in situ observations did not provide the spatial structure of the meteorological forcing over LNC, hence were not used to drive the lake models in this study. Rather, these data were used to validate and correct a 3-hourly data set, based mainly from the China Meteorological Forcing Data Set (CMFD), chosen to drive the lake models. CMFD covers 1979–2018 at 3-hourly intervals and with a horizontal resolution of 0.1° in longitude/latitude (available at <https://data.tpsc.ac.cn/en/>; He et al., 2020). It was produced through assimilating vast amounts of ground-based observations in addition to several remote-sensing and reanalysis data sets, and was documented to be a superior near-surface meteorological data set for land surface process and hydrology studies over China (Chen et al., 2011; L. Huang et al., 2017; A. N. Huang et al., 2019).

In this study, the lake models were run from May 1 to December 31, 2013. The models directly used the 3-hourly CMFD fields of surface downward shortwave and longwave radiation, air temperature at 2 m height, specific humidity at 10 m height, and surface air pressure. Figures 2a–2d compare the first four variables from CMFD with the in situ weather station data, and show excellent agreement between the two data sets. However, Figure 2e shows that CMFD underestimated the wind speed, especially during fall-winter (September–December). Following Lazhu et al. (2016), we introduced the following correction to the CMFD wind speed using the wind speed observed at the LNC weather station. This was achieved by establishing linear regressions between the daily wind speed from CMFD ( $X$ ) and in situ observations ( $Y$ ), derived as  $Y = 0.72X + 2.07$  for May–August and  $Y = 0.74X + 3.98$  for September–December, respectively. Both linear regressions are statistically significant at the 1% level (two-tailed  $t$ -test), and the corrected time series match well with the in situ observations (Figure 2e). The above linear relationships

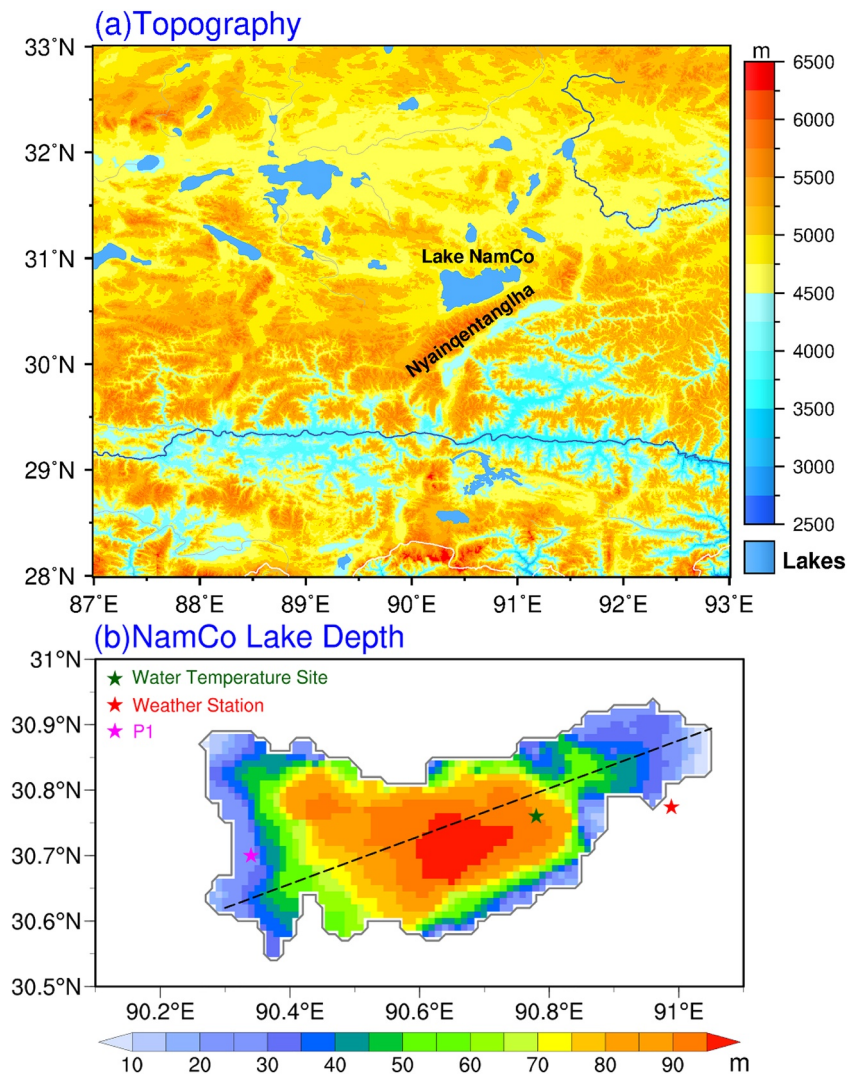


**Figure 1.** (a) Spatial distribution of land topography (unit: m) and lakes (blue colored areas) over the central TP. (b) Bathymetry of LNC (unit: m) with 1 km horizontal resolution. The darkgreen and red asterisks represent the LNC mooring site and the weather station, respectively. The dashed line denotes the southwest-northeast transection used in Figures 10 and 11. The magenta asterisk denote the selected site P1 (30.7°N, 90.34°E), with the water depth of 23.65 m, for plotting the time series shown in Figure 12.

were applied to the 3-hourly CMFD wind speed on the  $0.1^\circ \times 0.1^\circ$  grids. The wind direction, which is not available in CMFD, was determined by interpolating the wind direction from the ERA5\_Land reanalysis (with a horizontal resolution of 9 km, available at <https://cds.climate.copernicus.eu>; Copernicus Climate Change Service, 2019) onto the CMFD grids. This created a 3-hourly surface wind data set to drive the lake models. From Figure 2f, the ERA5\_Land wind direction matches well with the available in situ observations in representing the prevailing southwesterly wind. Figure 3 presents the monthly mean fields of this wind data set. It is notable that the dominant winds over LNC were southwesterly during May–December, resulting from the joint influence of the large-scale weather systems (summer southwestern monsoon and winter westerlies) and the local mountain-valley topography. The over-lake winds were stronger during September–December than during May–August. This was accompanied by the weakened radiation and the steady decrease in over-lake air temperature and atmospheric stability since September (Figure 2). We note that the ERA5\_Land wind speed was not used to derive the wind forcing because its time variability is less in agreement with the in situ observation than the CMFD wind speed (figure not shown).



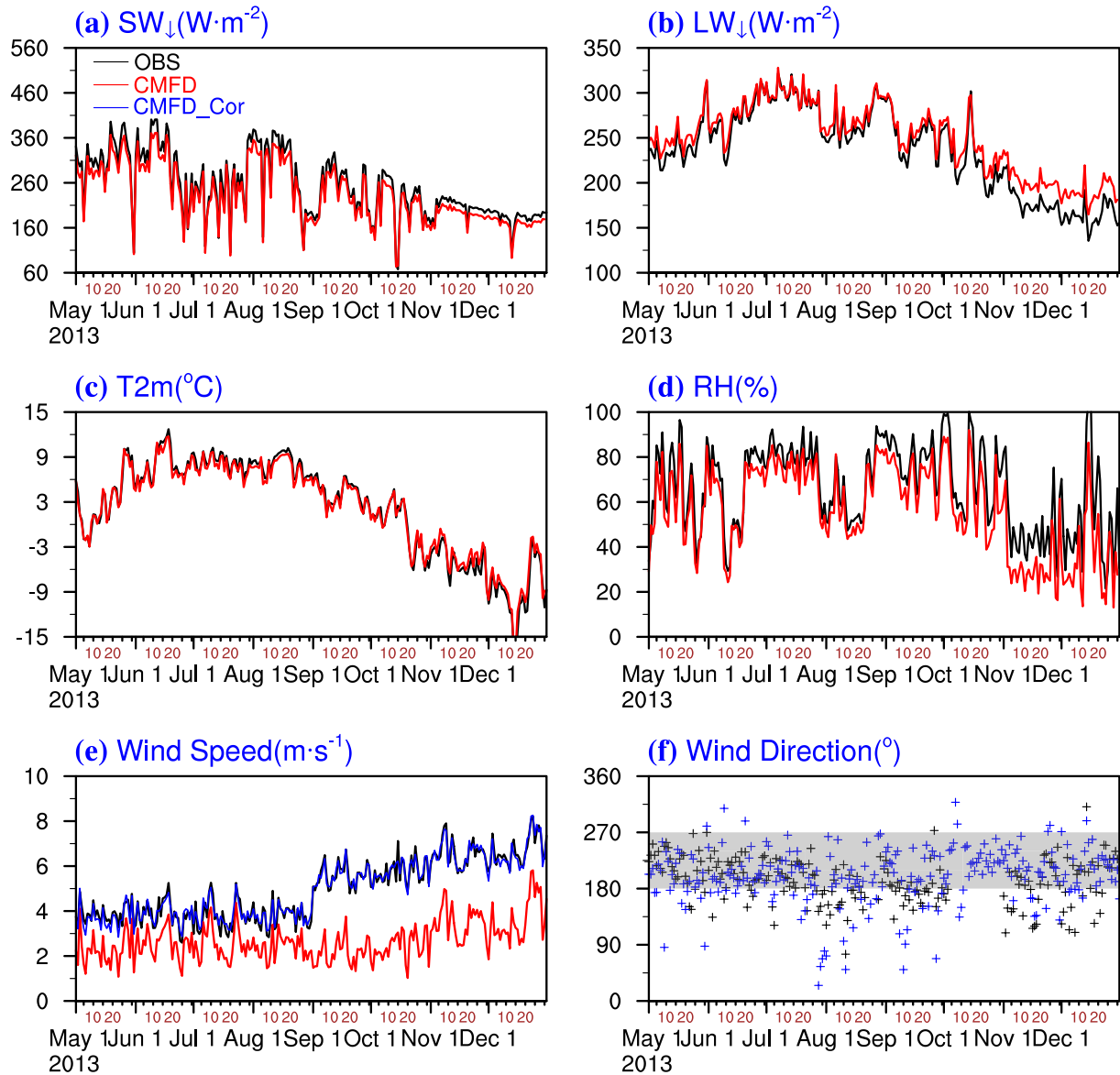


**Figure 2.** The daily in situ (black) and CMFD (red) of (a) surface downward shortwave radiation, (b) downward longwave radiation, (c) air temperature at 2 m above ground, (d) relative humidity at 10 m above ground, (e) wind speed and (f) wind direction at 10 m above ground during May 1 to December 31, 2013. The blue line in (e) and the blue markers in (f) denote the calibrated CMFD wind speed and wind direction, respectively.

## 2.2. Model Description and Experimental Design

The 3-D coastal ocean model POM solves nonlinear governing equations of lake water motions, temperature, and salinity using the finite difference method (Blumberg & Mellor, 1987; [https://www.ccpo.edu.edu/POMWEB/POM08\\_WAD/](https://www.ccpo.edu.edu/POMWEB/POM08_WAD/)). The horizontal space was discretized with a uniform grid spacing of 1 km, and the vertical discretization used 31 terrain-following sigma levels with finer resolution near the surface/bottom. The centers of the sigma levels are located at  $-0.0005$ ,  $-0.002$ ,  $-0.0055$ ,  $-0.009$ ,  $-0.0155$ ,  $-0.026$ ,  $-0.0365$ ,  $-0.047$ ,  $-0.0575$ ,  $-0.068$ ,  $-0.0785$ ,  $-0.089$ ,  $-0.0995$ ,  $-0.11$ ,  $-0.1205$ ,  $-0.131$ ,  $-0.1415$ ,  $-0.152$ ,  $-0.1625$ ,  $-0.173$ ,  $-0.1835$ ,  $-0.194$ ,  $-0.2045$ ,  $-0.262$ ,  $-0.3715$ ,  $-0.486$ ,  $-0.6$ ,  $-0.714$ ,  $-0.883$ , and  $-0.9975$ . The time steps for POM were set to 10 s for the external mode (depth-integrated flow and water level) and 300 s for the internal mode (depth-varying flow, temperature, and salinity). The Mellor and Yamada (1982) level 2.5 turbulence closure scheme (MY-2.5), combined with a wave-breaking parametrization scheme (Craig & Banner, 1994), was used to determine the vertical mixing parameters. The horizontal mixing was

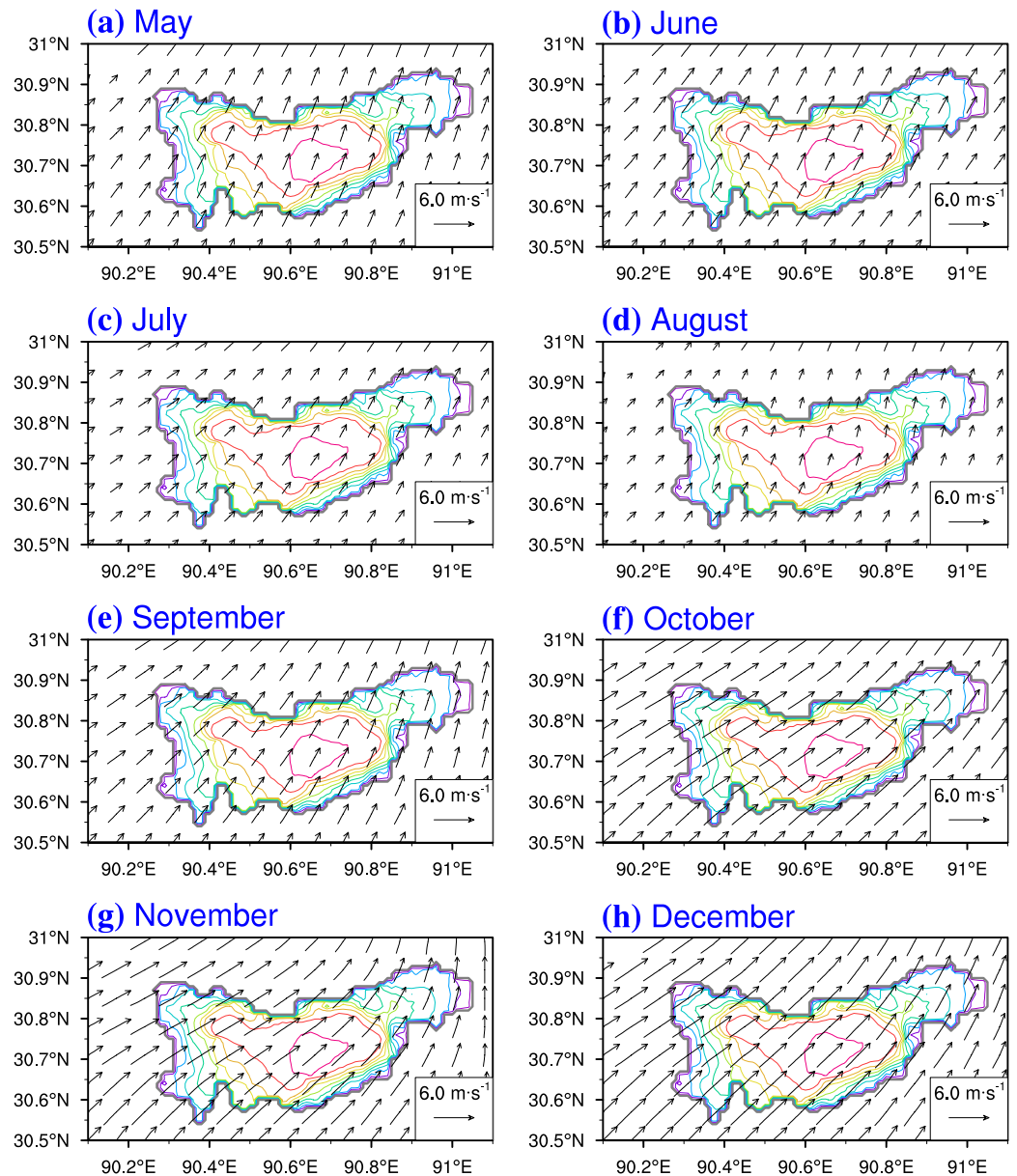


**Figure 3.** The monthly averaged wind fields at 10 m during May–December, 2013 from the calibrated CMFD datasets. The contour lines denote lake depths in 10 m intervals.

parameterized by a Laplacian scheme, and the horizontal viscosity and diffusivity are related to the strength of the horizontal shear of the velocity according to Smagorinsky (1963), with the constant parameter set to 0.2. The equation of state of Mellor (1991), which is an approximation of the complete UNESCO function, was used to calculate the water density as a function of temperature, salinity, and pressure. The model setup assumed that the lake water had no heat and salt exchanges with the closed lateral boundaries and lake bottom, and the velocity was free-slip along the lateral boundaries. The friction at the lake bottom was parameterized in quadratic form with the drag coefficient calculated according to:

$$C_{db} = \max \left[ \frac{\kappa^2}{\ln(z_b/z_{0b})^2}, 0.0025 \right] \quad (1)$$

where  $\kappa = 0.41$  is the von Karman constant,  $z_b$  is the distance from the bottom to the bottom layer center, and  $z_{0b} = 0.01$  m is the bottom roughness length.

The surface wind stress was calculated according to:

$$(\tau_x, \tau_y) = \rho_a C_d(u, v) \sqrt{u^2 + v^2} \quad (2)$$

where  $\tau_x, u$  ( $\tau_y, v$ ) are the eastward (northward) component of surface wind stress (in  $\text{N m}^{-2}$ ) and wind velocity (in  $\text{m s}^{-1}$ ) at 10 m height,  $\rho_a = 100P_a / [R_a(273.15 + T_a)]$  is the moist air density (in  $\text{kg m}^{-3}$ ),  $P_a$  is the input surface air pressure (in hPa),  $R_a = 287(1 + 0.608q_a)$  is the gas constant for moist air (in  $\text{J kg}^{-1} \text{K}^{-1}$ ),  $T_a$  is the surface air temperature (in degree Celsius),  $q_a$  is the specific humidity (in  $\text{kg kg}^{-1}$ ), and  $C_d = (7.5 + 0.67\sqrt{u^2 + v^2}) \times 10^{-4}$  is the wind drag coefficient (Garratt, 1977). For the heat flux at lake surface, the downward shortwave radiation ( $SW_{\downarrow}$ ) and longwave radiation ( $LW_{\downarrow}$ ) were specified according to CMFD, and 40% (60%) of the shortwave radiation were accounted for by the infrared (optical) band, with the vertical extinction coefficient assumed as  $2.85$  ( $0.1$ )  $\text{m}^{-1}$ . The value of the optical extinction coefficient was set according to the observed ranges of  $0.07$ – $0.17$   $\text{m}^{-1}$ , with the majority distributed within  $0.11$ – $0.13$   $\text{m}^{-1}$  (J. B. Wang et al., 2009). The upward longwave ( $LW_{\uparrow}$ ), sensible ( $SH_{\uparrow}$ ), and latent ( $LH_{\uparrow}$ ) heat fluxes were calculated according to (Verburg & Antenucci, 2010):

$$LW_{\uparrow} = \varepsilon \sigma T_w^4 \quad (3)$$

$$SH_{\uparrow} = \rho_a C_{pa} C_{sh} (T_w - T_a) \sqrt{u^2 + v^2} \quad (4)$$

$$LH_{\uparrow} = \lambda_v \rho_a C_{lh} (q_w - q_a) \sqrt{u^2 + v^2} \quad (5)$$

where  $\varepsilon = 0.98$  is the lake surface emissivity,  $\sigma = 5.67 \times 10^{-8} \text{Wm}^{-2} \text{K}^{-4}$  is the Stefan-Boltzmann constant,  $T_w$  is the surface water temperature (in degree Celsius),  $C_{sh} = 0.001$  ( $C_{lh} = 0.0016$ ) is the bulk constant coefficient of sensible (latent) heat,  $C_{pa} = 1005 \text{J kg}^{-1} \text{K}^{-1}$  is the specific heat of air,  $\lambda_v = 2.501 \times 10^6 - 2370T_a$  is the latent of vapourization (in  $\text{J kg}^{-1}$ ), and  $q_w$  is the saturated specific humidity (in  $\text{kg kg}^{-1}$ ). For all the above heat flux components, positive (negative) values mean that the lake water loses (gains) heat to (from) the atmosphere. The computation of heat fluxes involves the prognostic lake water temperature, and this has advantages over the prescribed or precomputed surface heat fluxes (Xue et al., 2015). Finally, in this application the influence of precipitation and surface evaporation on water level changes were not considered.

As an ice component is not included in the version of POM used for this study, the simulation was carried out from May 1 to December 31, 2013 to avoid dealing with the season with significant ice cover from January to April (Gou et al., 2017). The minimum water temperature was set to the freezing point temperature. POM was initialized with zero currents, a constant salinity of  $1.7 \text{g L}^{-1}$ , and a uniform temperature of  $1.96^\circ\text{C}$  which is the depth-averaged value of the rather homogeneous in situ lake water temperature on May 1, 2013.

Besides the 3-D POM, the 1-D WRF-Lake model was also used to simulate LNC. The 1-D model considered the snow, lake water/ice, and soil sediment processes within a lake column (e.g., Gu et al., 2015). WRF-Lake has undergone significant calibrations and has been applied in simulating the thermodynamics in LNC in offline or coupled settings (A. N. Huang et al., 2019; Wu et al., 2020). In this study, WRF-Lake is run in un-coupled mode for the same 8-month duration using the same initial condition and surface forcing as POM. The 1-D model with 25 vertical lake layers was applied on each horizontal grid of POM. In such a way, it obtained a 3-D representation of the LNC temperature variations that can be compared with the POM solution. Details of the 1-D model are described in Wu et al. (2020), including the adjustment of several key parameters, that is, parameterized surface roughness length (Subin et al., 2012), the temperature of maximum water density ( $T_{dmax} = 3.5^\circ\text{C}$ ), and a decreased light extinction coefficient with a scale factor of 0.8.

### 2.3. Analysis Methodology

For comparisons with the in situ observations, the lake temperature profiles simulated by POM and WRF-Lake at the LNC mooring site were linearly interpolated onto the depths of the observational data. The evaluation of the model simulated LST was carried out on bimonthly basis. For this, a total of 490 twice-daily MODIS images during May 1 to December 31, 2013 were used. As POM does not contain an ice model component, MODIS pixels with LST values less than  $0^\circ\text{C}$ , which mainly occurred at shallow coastal regions

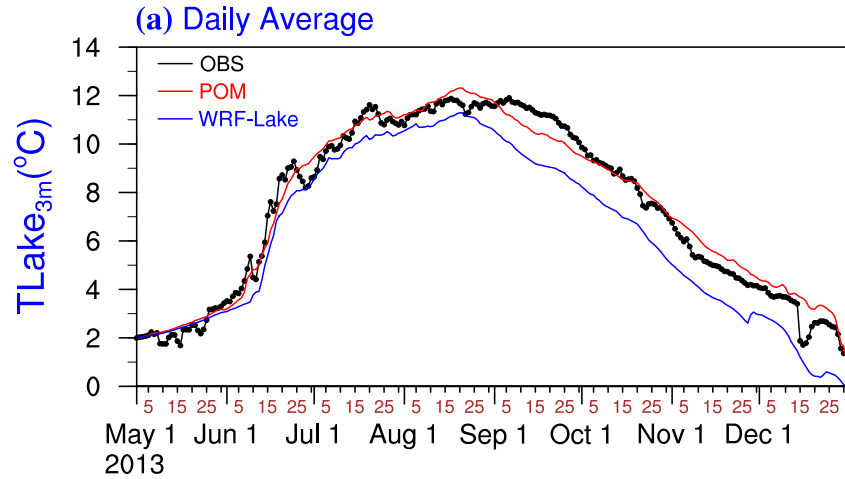


**Figure 4.** The daily lake temperature at 3 m depth ( $TLake_{3m}$ ) from the in situ measurements (black) and simulations of POM (red) and WRF-Lake (blue) at the mooring site during May 1 to December 31, 2013.

since late December, were excluded for comparison. The selected MODIS data were bilinearly interpolated onto the model grids (Shepard, 1968) and were then averaged to create bimonthly fields. The assessment used four statistical parameters, that is, the mean bias (BIAS), root-mean-square error (RMSE), Pearson temporal correlation (TC), and the Taylor score (TS), following A. N. Huang et al. (2019).

The heat balance for the lake water column in a given time interval can be expressed as (Titze & Austin, 2014; Wetzel & Likens, 2000):

$$\frac{\delta}{\delta t}LHC = SNHF + \theta_{hor} + \theta_{sed} \quad (6)$$

$$LHC = C_{pw} \int_0^h \rho_w(z)T(z)dz \quad (7)$$

$$SNHF = SW_{\downarrow} + LW_{\downarrow} - LW_{\uparrow} - SH_{\uparrow} - LH_{\uparrow} \quad (8)$$

where  $\delta LHC/\delta t$  (in  $W m^{-2}$ ) is the rate of heat content change within the lake column of unit area, which is balanced by the surface net heat flux ( $SNHF$ ), horizontal heat transport due to advection and mixing ( $\theta_{hor}$ ), and the conductive heat exchange between lake water and bottom sediments ( $\theta_{sed}$ ).  $C_{pw} = 4180 J kg^{-1} K^{-1}$  is the specific heat of water,  $\rho_w(z)$  is the water density (in  $kg m^{-3}$ ),  $h$  is the bottom lake depth (in m),  $T(z)$  (in  $^{\circ}C$ ) is the lake temperature at depth  $z$  (in m). In POM,  $\theta_{hor}$  is the sum of the lateral heat transports due to advection and mixing, and can be calculated according to  $\theta_{hor} = \delta LHC/\delta t - (LHC + SNHF)$  due to the use of adiabatic bottom boundary conditions. Positive  $SNHF$  and  $\theta_{hor}$  mean that the local lake column gains heat. The above heat budget components were firstly calculated based on the daily POM output and are then averaged over bimonthly intervals for analysis. The heat budget analysis was not performed for November–December due to the missing ice thermodynamics in POM.

### 3. Results and Discussion

#### 3.1. Lake Surface Temperature and Lake Column Heat Balance

Figure 4 shows the daily time series of the lake temperature at 3 m depth ( $TLake_{3m}$ ) from the in situ observations and simulations with POM and WRF-Lake, and Figure 5 presents the related quantitative statistics to evaluate the model accuracy against observations. The statistical values were estimated for the entire time series, and also bi-monthly. Since May 1, the observed  $TLake_{3m}$  at the LNC mooring site exhibited a continuous warming from 2 to 11.9 $^{\circ}C$  until late August, and then a gradual decrease to 1.35 $^{\circ}C$  by the end of December. POM well reproduced the observed seasonal evolution of  $TLake_{3m}$ , but failed to capture most of the observed synoptic events such as rapid coolings. By comparison, WRF-Lake underestimated  $TLake_{3m}$ , especially since September during the lake destratification/overturning phase. WRF-Lake exhibited large negative BIAS of  $-1.74^{\circ}C$  ( $-1.45^{\circ}C$ ) in September–October (November–December), and BIAS (RMSE) of



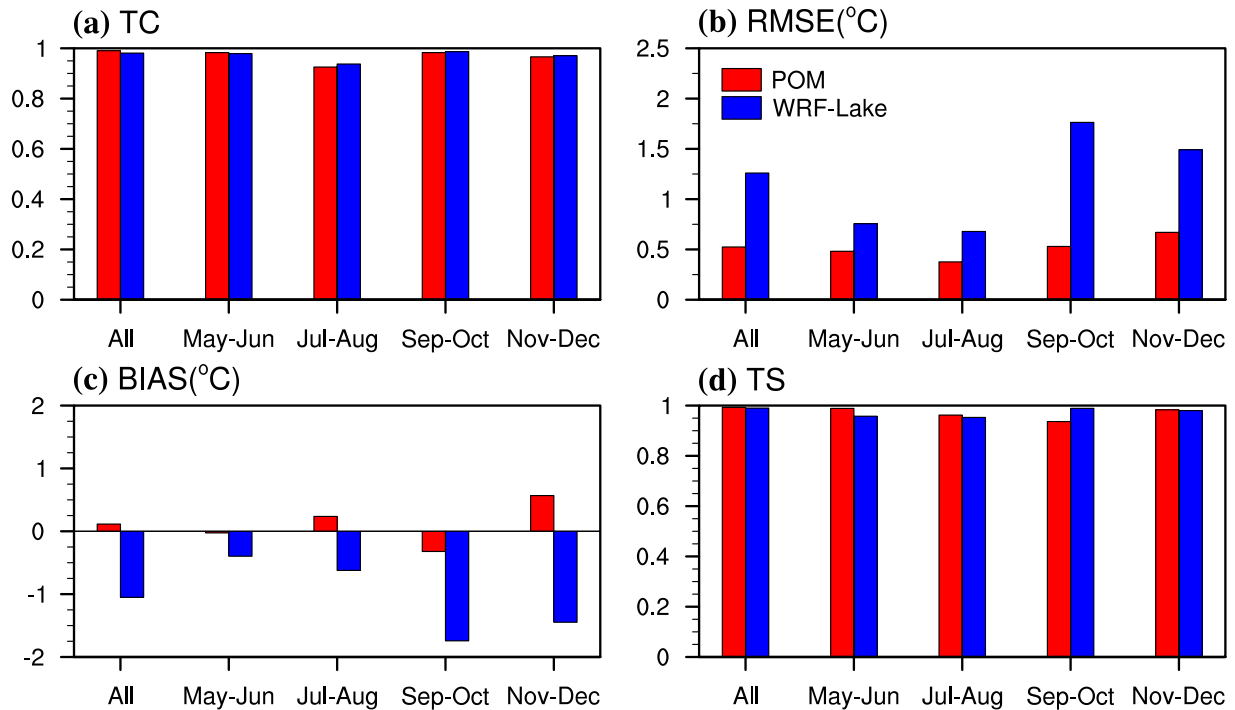


**Figure 5.** (a) Temporal correlation (TC), (b) RMSE, (c) BIAS, and (d) Taylor score (TS) for the daily lake temperature at 3 m depth ( $TLake_{3m}$ ) from POM (red) and WRF-Lake (blue) relative to the mooring observations. The statistical values are estimated for the entire time series during May–December 2013 and for bimonthly periods.

–1.0°C (1.25°C) for the whole simulation period. POM showed a slight warm BIAS of 0.12°C with RMSE of 0.52°C for the whole simulation period. Both POM and WRF-Lake yielded TC and TS values exceeding 0.95, suggesting their similar capability in reproducing the daily  $TLake_{3m}$  variability.

Next, we compare the bimonthly averaged LST from the two models and the MODIS data, and discuss the causes of the LST variations through analyzing the lake column heat balance based on the POM simulation. Figure 6 shows the spatial maps of the LST; Table 1 lists the mean and RMSE values of LST; and Figures 7 and 8 present the heat budget components ( $\delta LHC/\delta t$ ,  $SNHF$ ,  $\theta_{hor}$ ) based on POM simulation over LNC and at the mooring site, respectively. When comparing the mean and RMSE values listed in Table 1, one should bear in mind that LST values from satellite remote sensing are usually lower than the in situ observed values due to the cool skin effects, by about 0.8–1.9°C in many cases (Hook et al., 2003; Ke & Song, 2014). In the following, the four bimonthly durations are discussed successively.

According to the POM solution, during May–June, the lake column heat content increased across the whole LNC (Figure 7a) corresponding to the positive surface net heat flux (Figure 7b). As the model’s initial thermal state was nearly uniform in space and the horizontal variation of the surface net heat flux was small (Figure 7b), the modeled LST rose higher over the shallower areas than in deeper regions (Figures 6a–6c). This created the cross-isobath LST gradient that was also documented in many other large lakes with sloping bathymetry (e.g., Boyce et al., 1989; Rao et al., 2004). Previous studies (Beletsky & Schwab, 2001) showed that the cross-isobath temperature gradient not only enhanced the horizontal temperature diffusion, but also generated baroclinic circulation, both contributing to the redistribution of heat. In the POM solution, during May–June, the surface currents consisted of eastward flow in the western part and a weak cyclonic gyre in the mid-lake region (Figure 6b); and around the outer edge of the cyclonic gyre in the deep central basin (Figure 7c), the lateral heat transport ( $\theta_{hor}$ ) was positive, acting to increase the water column heat content (Figure 7a); while the water column in the western and southeastern coast lost heat, indicating the lateral heat transport from the coastal to central lake regions. As a result, the POM solution showed a less pronounced nearshore-offshore LST gradient, hence a warmer “cold pool” in the central deep area than the WRF-Lake solution (Figures 6b and 6c). The negative  $\theta_{hor}$  along the western coast can be mostly

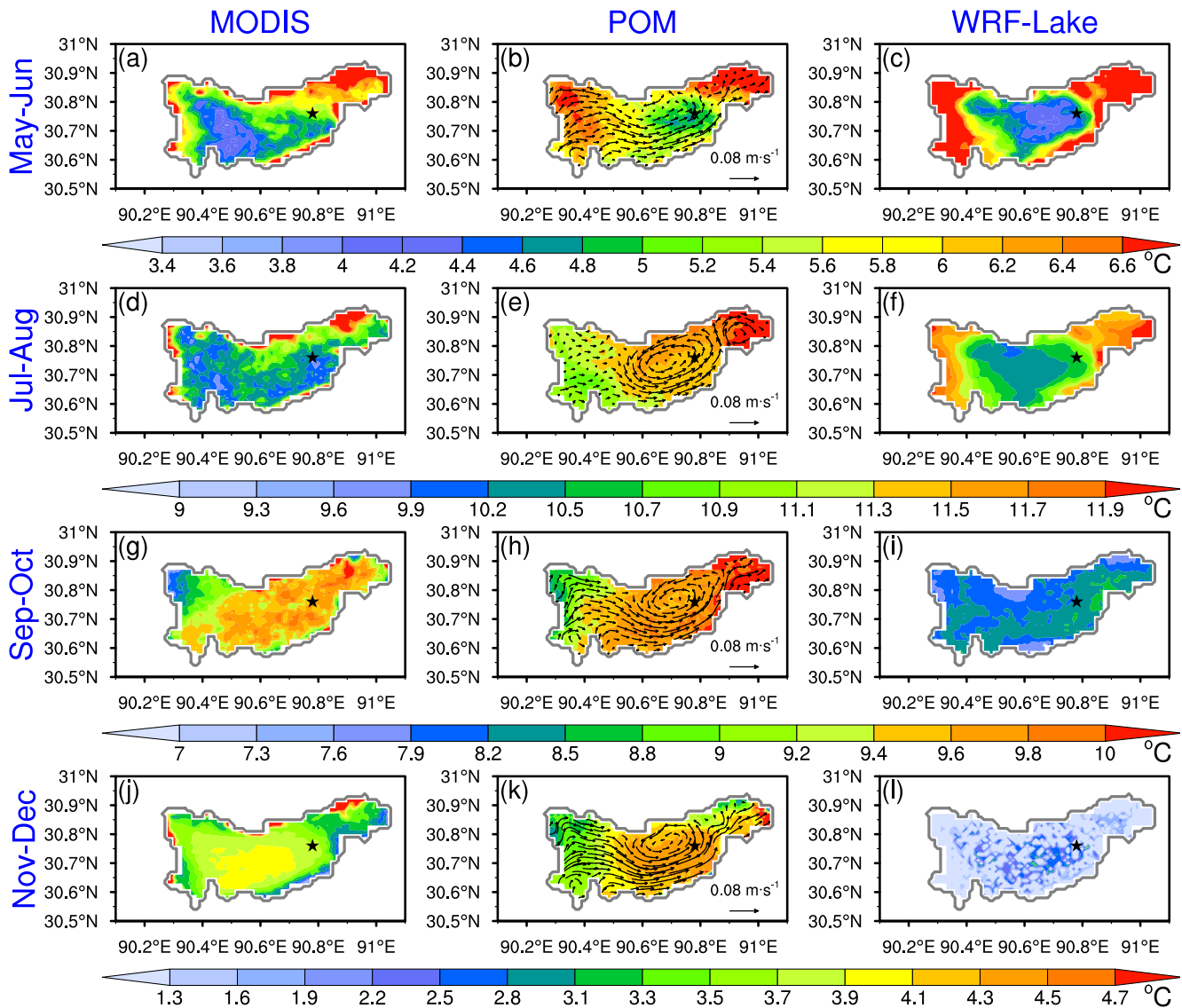


**Figure 6.** The bimonthly averaged LST during May–December in 2013 from (left column) MODIS, (middle column) POM, and (right column) WRF-Lake. The vectors in the middle column represent the water currents averaged over the surface layer (0–3 m). The black asterisks denote the mooring site.

attributed to the wind-driven upwelling, to be discussed in Section 3.4. At the mooring site, the horizontal heat exchanges in POM contributed to approximately 17% of the bimonthly increase in lake column heat storage during May–June (Figure 8). Relative to MODIS, POM and WRF-Lake both obtained slightly higher lake-averaged LST, by 0.23 and 0.30°C, with same RMSE of 1.78°C (Table 1).

**Table 1**  
The Bimonthly Area-Averaged Lake Surface Temperature (LST, Unit: °C) From MODIS Observation and POM/WRF-Lake Simulations

	May–June		July–August		September–October		November–December	
	LST	RMSE	LST	RMSE	LST	RMSE	LST	RMSE
<b>MODIS</b>	5.74	–	10.74	–	9.38	–	3.69	–
<b>POM</b>	5.97	1.78	11.40	1.04	9.60	0.47	3.99	0.93
<b>WRF-Lake</b>	6.04	1.78	11.01	0.93	8.20	1.30	1.09	3.05

Note. RMSE denotes the root-mean-square errors (RMSE, unit: °C) between the simulations and MODIS data.

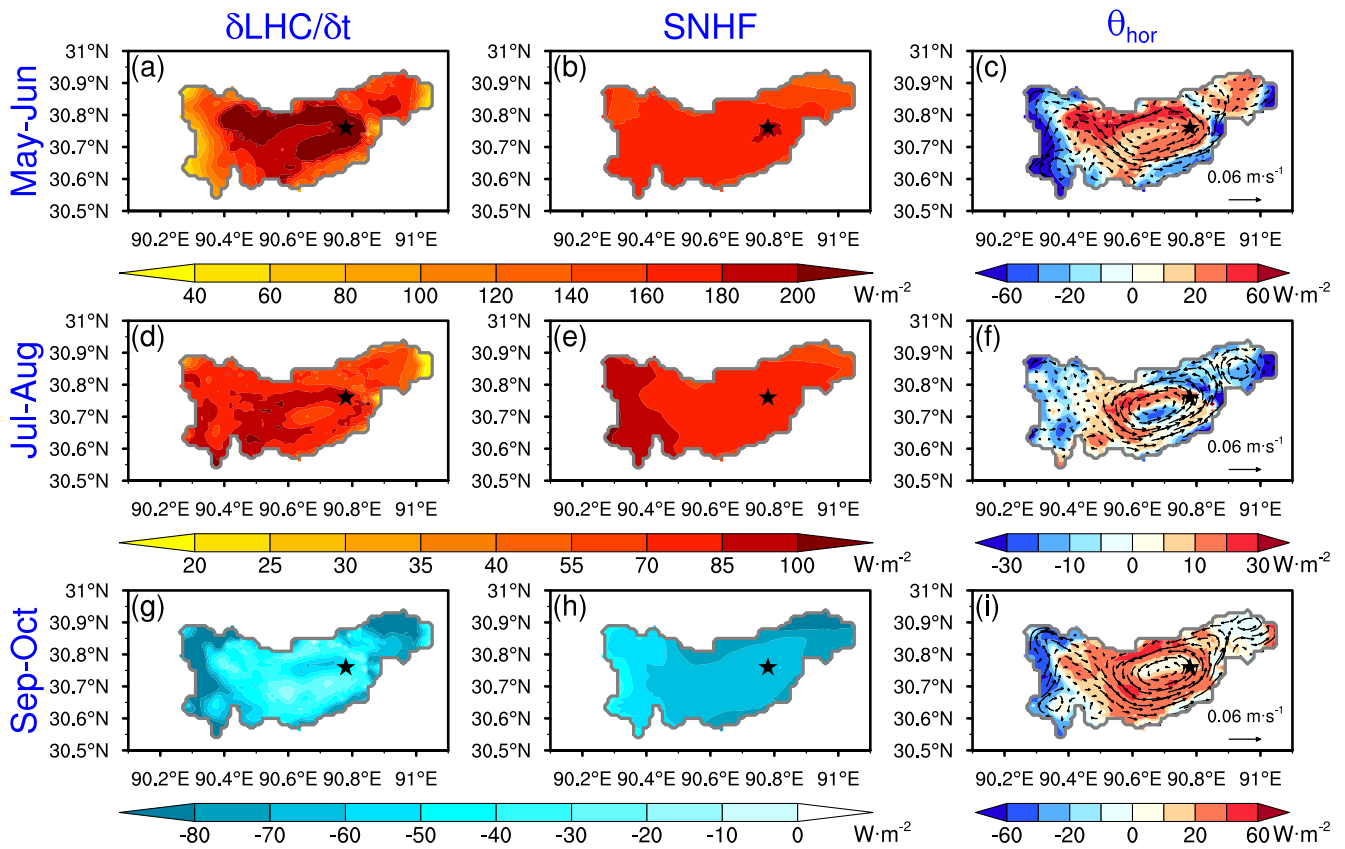


**Figure 7.** The bimonthly averaged heat budget components (unit:  $W\ m^{-2}$ ) based on POM: (left column) rate of change in lake heat content  $\delta LHC/\delta t$ , (middle column) surface net heat flux SNHF, and (right column) horizontal heat exchange  $\theta_{hor}$  during May–October 2013. The vectors in the right column represent the depth-averaged currents.

According to POM, during July–August the persistent heat input at the lake surface further increased the lake column heat storage and LST (Figures 7d and 7e); LNC became fully stratified with a relatively warm homogeneous epilimnion (to be discussed in Section 3.3), and the LST increased from the western to the eastern lake regions. POM roughly captured the observed spatial variability of LST, while WRF-Lake still obtained pronounced nearshore-offshore LST gradient as in May–June. This difference can again be related to the horizontal heat exchange included in the POM simulation. The modeled lake circulation featured an anti-cyclonic gyre in the eastern basin and a cyclonic gyre in the main basin (Figure 6e), and the lateral heat transport on the pathway of the main gyre was less than that in May–June (Figure 7f). At the mooring site,

the horizontal heat exchanges accounted for  $\sim 19\%$  of the increase in lake column heat content in the POM solution (Figure 8). Relative to MODIS, POM and WRF-Lake both obtained higher lake-averaged LST, by 0.66 and 0.27°C, with similar RMSE of 1.04 and 0.93°C, respectively (Table 1).

During September–October, the modeled heat storage of LNC decreased due to the heat loss at the lake surface (Figures 7g and 7h). The intensified over-lake turbulent sensible/latent heat loss can be related to the strong winds and the higher temperature and humidity of surface lake water than that of surface air. From July–August to September–October, the area-averaged LST from POM decreased from 11.40 to 9.60°C, comparable with the MODIS data from 10.74 to 9.38°C. WRF-Lake obtained a much larger decrease from 11.01 to 8.20°C (Table 1), and this can be related to the previously reported “rapid autumnal cooling” issue in the Hostetler-based model (Martynov et al., 2010). Both MODIS and POM showed that the LST increased from northwest to southeast (Figures 6g

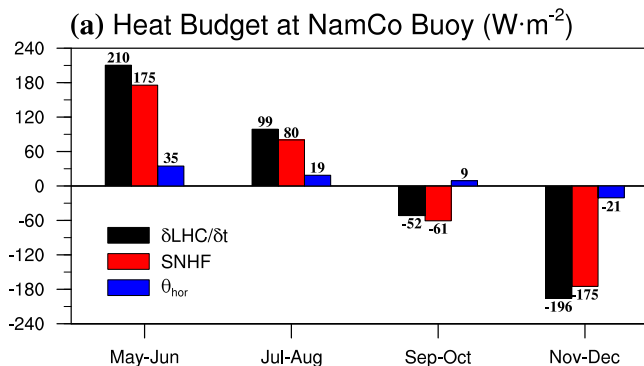


**Figure 8.** Same as Figure 6, but for the heat budget at the LNC mooring site.

and 6h). This can be partly attributed to the eastward warm water aggregation by the prevailing southwesterly winds, especially during October when the lake circulation was largely influenced by winds under the weakly stratified condition (to be discussed in Section 3.3). This spatial LST gradient was not captured by WRF-Lake (Figure 6i). The horizontal heat transport was basically from the western coastal to central lake regions (Figure 7i). At the mooring site, the modeled lateral heat transport counteracted the surface heat loss (Figure 8), leading to more realistic decrease of LST in POM than in WRF-Lake (Figure 4).

During November–December, the modeled LST further decreased over the entire LNC (Figures 6j–6l). According to MODIS and POM, over the central deep region LST decreased slower, and was approximately 0.8 and 1.2°C higher than that in the coastal areas. The higher LST in MODIS and POM in the deep central region can be related to the epilimnetic heat loss being partly compensated by the warm hypolimnion as a consequence of the wind-induced mixing or the gravitationally driven vertical convection. According to POM, the lateral processes caused heat loss at the mooring site (Figure 8). WRF-Lake also produced much higher LST in the middle lake than coastal regions. For the area-averaged LST, POM obtained a value of 0.30°C higher, whereas WRF-Lake obtained a value of –2.6°C lower, than that from MODIS. The excessively low LST in WRF-Lake can be attributed to the less heat retention in the central lake region during the previous seasons (Figures 6c, 6f, and 6i). During autumn–winter, POM obtained the spatial distribution of LST in better agreement with MODIS than WRF-Lake, as indicated by the much lower values of RMSE (Table 1).

The above analysis revealed that the thermodynamics in LNC existed large horizontal variabilities during the ice-free period and hence suggested that both the local lake–air heat flux and lateral heat redistribution should be considered when modeling such large deep dimictic lakes. Regarding the contributions of advection and mixing to the lateral heat transport, analysis results (figure not shown) suggested that the values and spatial patterns of  $\theta_{hor}$  shown in Figure 7 were mainly due to advection; the lateral heat transport due to mixing showed less spatially structure and made secondary contribution, except at locations with large lake temperature gradients.

### 3.2. Vertical Profiles of Lake Temperature

Figures 9a–9c show the evolution of water temperature profiles at the mooring site from the in situ observations and simulations with POM and WRF-Lake. According to the three statistical quantities (Figures 9d and 9e), overall, POM performed much better than WRF-Lake in reproducing the seasonal and synoptic variations of the vertical thermal structure. In particular, the RMSE values of the water temperature from POM were within the reasonable range of 0.40–1.19°C, while the maximum RMSE value from WRF-Lake reached 2.40°C (Figure 9e).

The onset (end) of lake thermal stratification is defined as the first (last) date from which the temperature differences between 6 and 66 m depths are greater than 1°C (J. B. Wang et al., 2019). According to observations (Figure 9a), (a) the lake water temperature was slightly lower at surface than in deeper layers until the lake thermal stratification established on June 4; (b) as the result of the persistent radiative heating from June to early September (Figures 2a and 2b), the epilimnion gradually warmed and the thermocline deepened, with the maximum mixed layer depth exceeding 30 m; (c) since then, due to the increasing surface net heat loss and enhanced vertical mixing, the mean epilimnetic temperature gradually descended to ~5.5°C, and the mixed layer continually deepened to ~50 m at the end of the destratification phase (November 7); and (d) during the subsequent lake overturning phase, temperature of the entire water column became nearly uniform and continually decreased until LST reached  $T_{dmax}$  around mid-December, after which LST dropped below  $T_{dmax}$  to form the typical inverse thermal stratification that was gravitationally stable.

According to POM (Figure 9b), the establishment of thermal stratification was on June 7, in better agreement with the observed date of June 4 than June 15 predicted by WRF-Lake. In the POM solution, the lateral heat transport was positive at the mooring site (Figures 7c and 8), in favor of an earlier development of stratification. POM showed deficiency in modeling the temperature of metalimnion, and the largest errors occurred at the thermocline regions, with the RMSE values up to 1.19°C at 21 m depth (Figure 9e). POM predicted a shallower mixed layer and a more diffuse thermocline compared with observations, and similar deficiencies were identified in previous POM applications in Lake Michigan and Lake Erie (Beletsky et al., 2006, 2013). Additionally, POM failed to reproduce the observed episodes of rapid thermocline

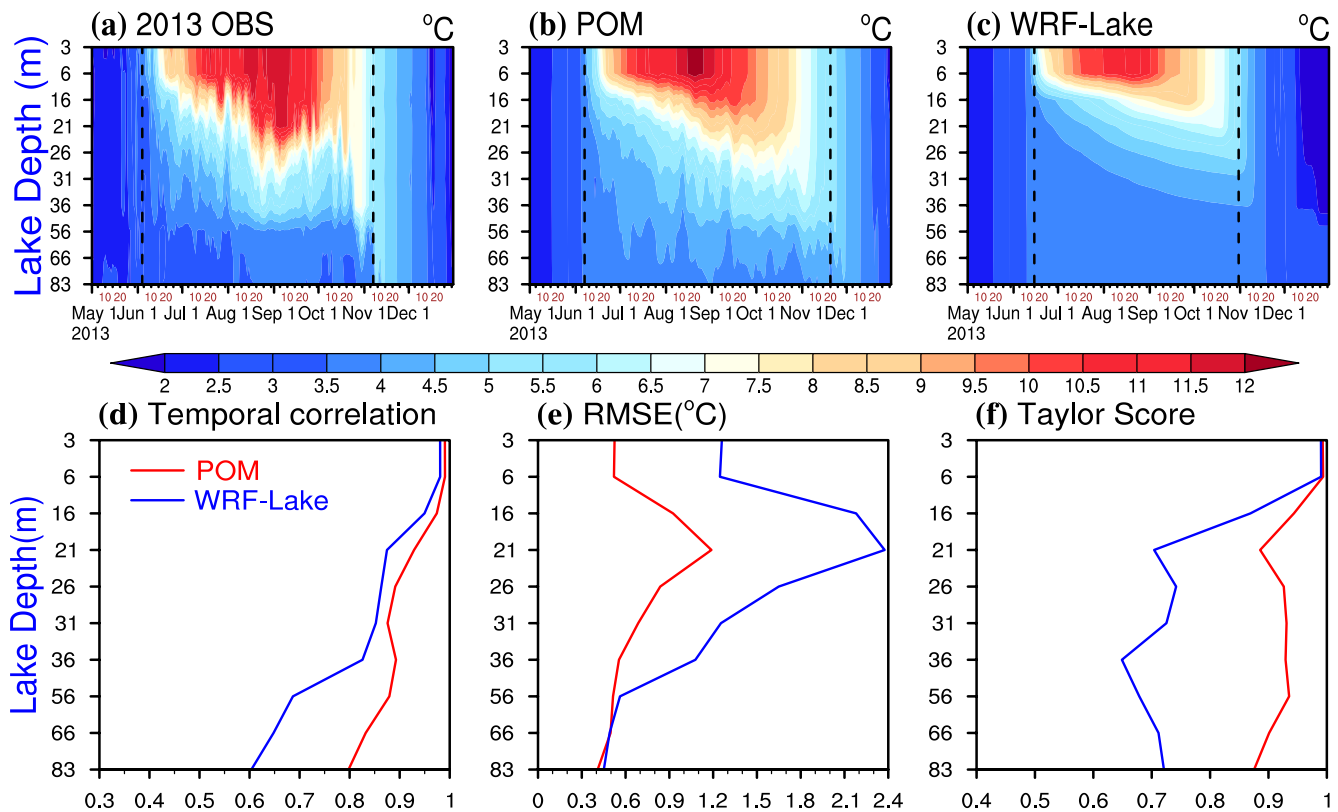


**Figure 9.** Time-depth variations of the daily mean lake temperature from (a) observations, (b) POM, and (c) WRF-Lake at the LNC mooring site. The vertical distributions of the (d) temporal correlation (TC), (e) RMSE, and (f) Taylor score (TS) for the daily lake water temperature during May–December in 2013 from POM (red) and WRF-Lake (blue) relative to observations at 10 levels. The black dashed lines in (a–c) indicate the onset and end of lake thermal stratification.

oscillations that occurred at 21–31 m depths during late August, which were likely due to the internal wave activities (J. B. Wang et al., 2019). POM predicted the date of destratification on November 20, nearly 2 weeks behind the observed date of November 7. The above deficiencies may be attributed to inaccuracy in surface forcing, the simplified wind drag coefficient that depends on wind speed only, and also the POM's imperfect numerics (i.e., numerical diffusion) or the missing physics (i.e., wave-induced mixing, Langmuir circulation, and internal waves) (Huang & Qiao, 2010; Kantha & Clayson, 2004; Langmuir, 1938). By comparison, WRF-Lake predicted a too early date of destratification on October 31, and colder water column temperature during winter, likely due to the less heat retention during the previous spring-summer.

### 3.3. Thermal Structure and Circulation Based on the POM Simulation

As documented in previous studies, water temperature and circulation in large lakes show pronounced spatiotemporal variabilities due to the multi-scale thermo-hydrodynamics (e.g., Hutter, 1984; Mortimer, 1987, 2004; Nyamweya et al., 2016; Schwab & Beletsky, 2003). LNC is a large dimictic lake with a high altitude (4,731 m). Previous studies (e.g., J. B. Wang et al., 2019) showed that LNC is well mixed both horizontally and vertically with a temperature less than  $T_{dmax}$  before May, and features complex limnological phenomena during May–December, that is, the spring TB, summertime stratification, autumnal destratification and winter turnover processes.

The thermal structure and circulation based on the POM simulation are presented and discussed below. Figures 10 and 11 show the monthly lake temperature along and horizontal currents normal to a south-west-northeast transection, and horizontal distributions of the depth-averaged water currents and water level. As the solar radiation increased from spring to early summer (Figures 2a and 2b) and the radiative penetration decreased with depth, the upper water body received large portions of the incoming radiation and was first heated toward  $T_{dmax}$ . During this period, the epilimnion became denser, hence continuously



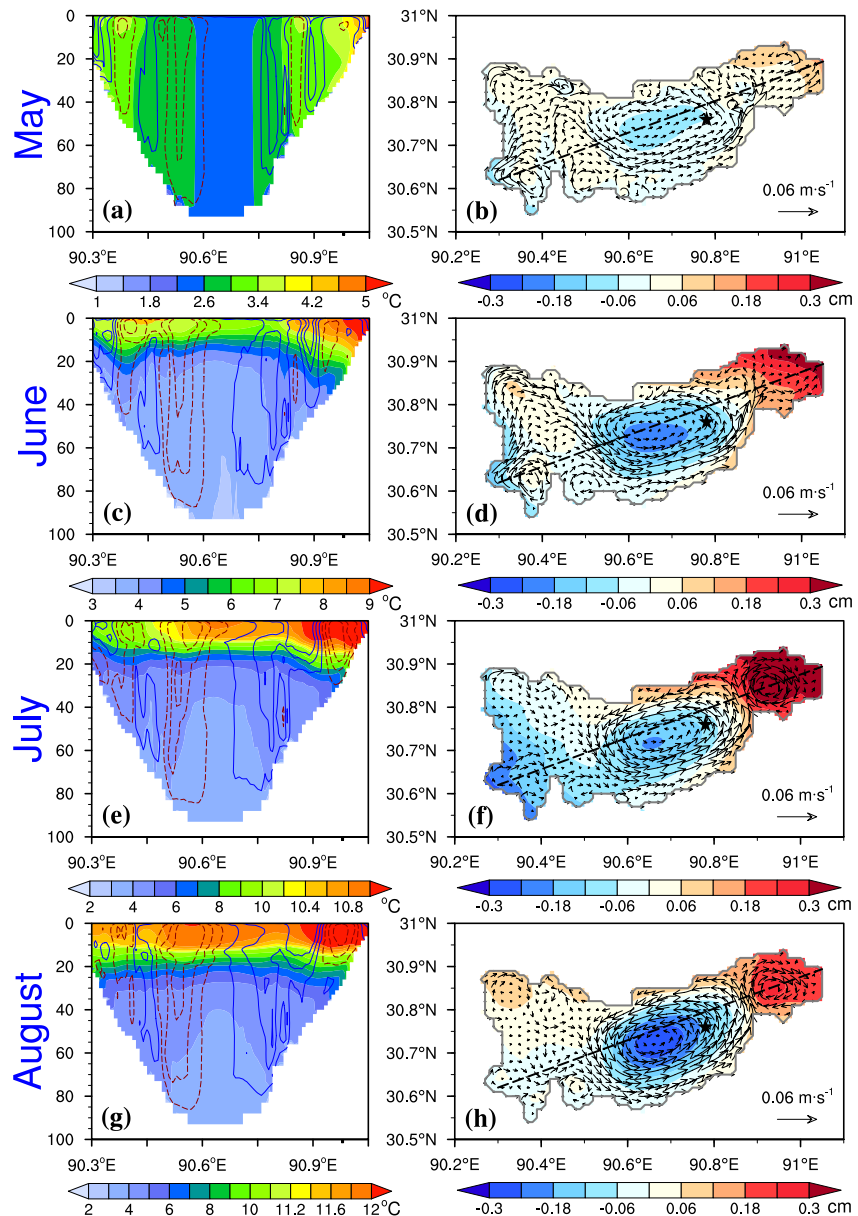


**Figure 10.** Monthly averaged (left column) lake temperature (color shading) along the southwest-northeast transection and horizontal currents (contours) normal to this transection, and (right column) lake water level (color shading) and depth-averaged currents (vectors) during May–August in 2013. In the left panels, the contours have intervals of  $0.01 \text{ m s}^{-1}$ , with solid (dashed) contours denoting currents in northwestward (southeastward) direction. In the right panels, the black dashed lines denote the transection position and the black solid asterisks represent the location of LNC mooring.

sank and mixed with the colder water below. This led to homogeneous heating of the water column until the hypolimnetic temperature reached  $T_{\text{dmax}}$  and the water column became gravitationally stable and stratification began to develop. In May, a weak thermal stratification was firstly established around the coastal regions in LNC, while the convective heating still occurred in the deep mid-lake regions, and the TB existed in between (Figure 10a). The main circulation was the cyclonic gyre between the TB zone and the deep mid-lake, corresponding to a horizontal gradient of water level decreasing from the TB zone to the mid-lake (Figure 10b). This cyclonic gyre was quite uniform in the vertical space (Figure 10a), and tended to be in parallel with the TB hence did not make significant contributions to the cross-TB heat transport from coastal to mid-lake regions. Note that the northward (eastward) alongshore currents and the depressed (elevated) water level were also developed in the western (eastern) shallow coastal waters (Figure 10b).

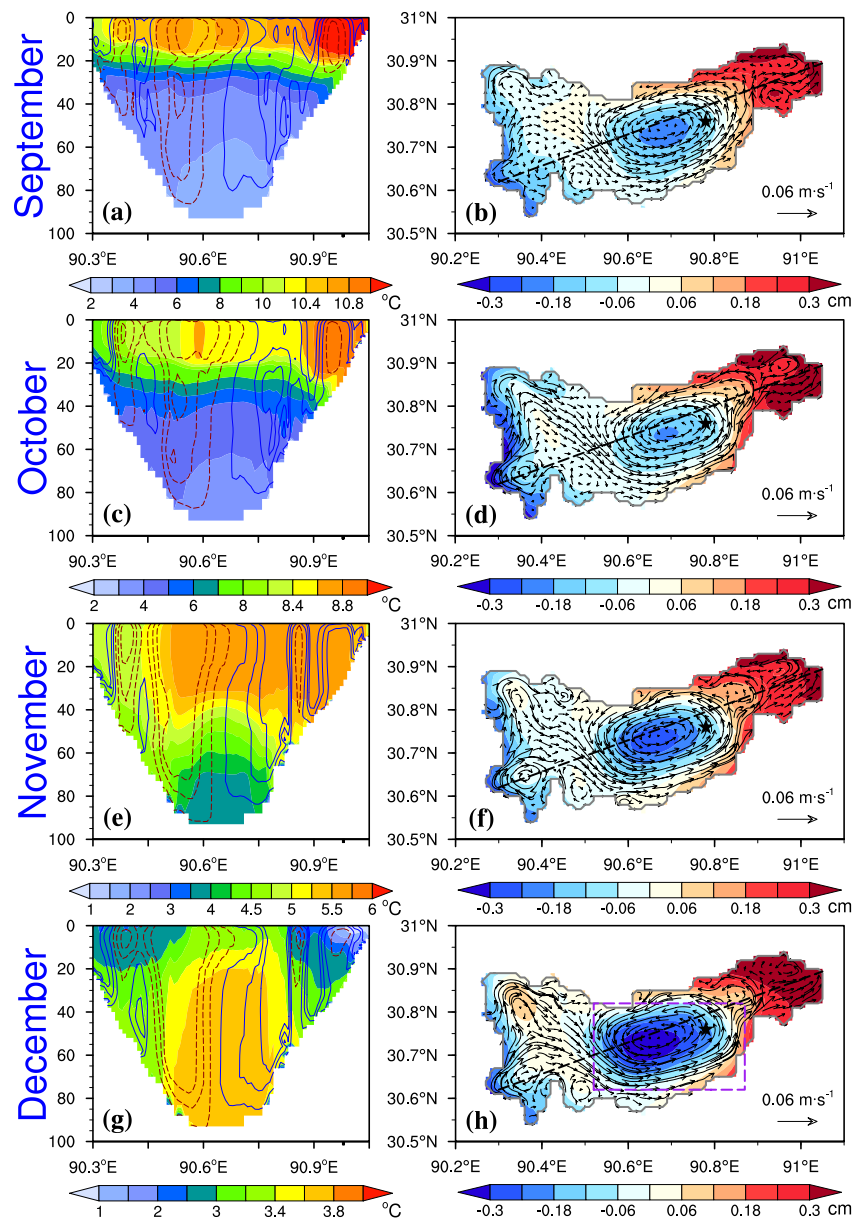


**Figure 11.** Same as Figure 10 except for during September–December, 2013. The purple rectangle box outlines the central lake region (30.62–30.82°N, 90.52–90.87°E) used for analysis shown in Figure 13.

From June to August, the modeled thermal stratification was developed across LNC. In June, the horizontal gradient of water temperature mainly existed in the upper 20-m layer (Figure 10c). In the deep mid-lake, the upper layer was colder than in shallow regions and the thermocline showed a dome shape, resembling that in the deeper basins of Lake Michigan and Lake Erie (Beletsky & Schwab, 2008; Beletsky et al., 2013; Schwab et al., 1995). The doming thermocline created an internal pressure gradient between the central and coastal regions and contributed to the mid-lake cyclonic circulation (Figure 10d). In the western part, there existed a strong northward depth-averaged current turning off from the coast and feeding into the southeastward current, the water level showed low values and the isotherms tilt upward toward the western coastal region (Figures 10c and 10d), and this can be related to the offshore Ekman transport and coastal upwelling due to the prevailing southwesterly wind (Figure 3b). The above circulations showed evident vertical structure, with stronger flows occurring in the upper layer (Figure 10c). The surface flow acted to redistribute heat within the lake and finally led to the warm water aggregation in the eastern shallow basin. In July and

August, the upper layer further got warmed and penetrated deeper, and the highest temperature still appeared and reached the deepest in the eastern region (Figures 10e and 10g). In the mid-lake, the thermocline became flat and no longer showed the dome shape, while in the eastern shallow region, a warm lens of water was formed with isotherms showing a bowl shape (Figures 10e and 10g). In the western region, the circulation became rather weak associated with the weakening of the southwesterly wind (Figures 10f and 10h). In July and August, the gyres and distribution of water levels in the central and eastern regions were similar to that in June. The depth-averaged flow featured two contour-rotating gyres: a cyclonic gyre in the central region and an anti-cyclonic gyre in the eastern shallow region (Figures 10f and 10h).

In September, LNC entered the autumnal destratification phase due to the decreased solar radiation and intensified turbulent sensible/latent heat loss (Figure 2). Toward the western coast, the thermocline showed an upward tilt (Figures 11a), and the northward flow and depression of water level appeared (Figures 11b), in correspondence to upwelling due to the strengthening of the southeasterly wind (Figure 3e). In the central region, the cyclonic circulation still existed but was weaker than in August corresponding to the decreased water level gradient (Figures 11b). In the eastern region, the water level was elevated around the coastal region and sustained the eastward alongshore current (Figures 11b). In October, the upper layer further got cooler and penetrated deeper (Figures 11c), and circulation and water level distributions were similar to that in September, except for the indication of stronger upwelling (Figures 11d) that can be related to the further strengthening of the southwesterly wind (Figure 3f). The northward depth-averaged current turned off from the western coast and fed into the southeastward current in the western part of the mid-lake region (Figures 11d). This relatively strong southeastward current must be primarily driven by wind because the water level did not show pronounced spatial gradient.

In November, as the lake continued losing heat to the atmosphere, the upper layer further deepened (Figures 11e). In the upper 40 m, the western region cooled off and de-stratified faster, likely due to the continuous upwelling by the southwesterly wind (Figure 3g). The depth-averaged circulation and the distribution of water level (Figures 11f) were overall similar to that in October. In December, the water temperature in the western and eastern shallow regions dropped faster than in the central deep region (Figures 11g). As a result of the preferential cooling in the shallow regions, the autumn thermal bar was firstly formed here and then moved progressively to the deeper regions, with LNC entering the overturning phase. Averaged over December, the vertical distribution of water temperature across LNC featured a weak inverse thermal stratification with colder water lying above the warmer water (Figures 11g). The depth-averaged circulation and the distribution of water level (Figures 11h) were similar to that in September and October. In both November and December, the horizontal currents showed less vertical shear due to the reduced stratification (Figures 11e and 11g), compared with during June–October.

### 3.4. High-Frequency Variations Related to Wind-Driven Upwelling

The above discussions on the monthly mean fields suggested that upwelling along the western coast of LNC was evident in June and September–November due to the presence of strong southwesterly wind during these months. To examine the details of time variations, Figure 12 shows the time series of the three terms of the water column heat budget, water level, LST, and wind speed and direction during October–November 2013, at a location P1 shown in Figure 1 with the water depth of 23.65 m. During these 2 months, the southwesterly wind prevailed with daily mean speed above  $6 \text{ m s}^{-1}$ , and the water level at P1 was on average  $\sim 0.2 \text{ cm}$  below the mean water level (Figures 12b–12d). However, there was an obvious spike around November 18, occurred when the southwesterly wind weakened and shifted to easterly that favored downwelling along the western coast. The simultaneous  $\theta_{hor}$  and water level showed high-frequency oscillations due to the synoptic-scale variations of wind speed, accompanied by LST fluctuations on top of a trend of gradual decrease (Figures 12a–12c). This suggested that the lateral heat transport integrated for the water column dominated the high-frequency variations of the total heat content change ( $\delta LHC/\delta t$ ), and it was not necessarily always negative for this period. Meanwhile, the surface net heat flux ( $SNHF$ ) steadily maintained negative and relatively smaller values (Figure 12a).

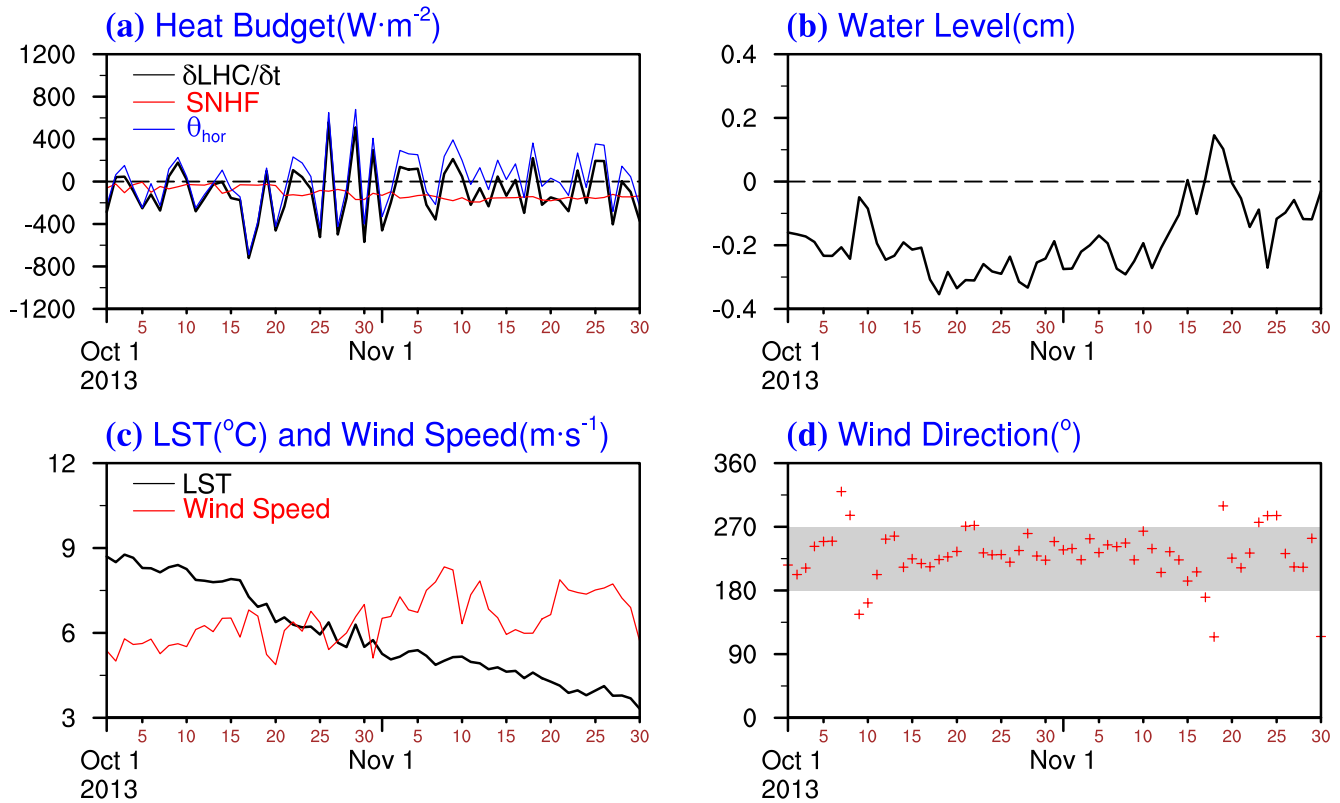


**Figure 12.** Daily time series of (a) the three heat budget terms, (b) water level, (c) lake surface temperature and wind speed, and (d) wind direction at P1 during October–November, 2013. In (d), wind direction is calculated in 0–360° clockwise from due north, and the gray shading range of 180–270° corresponds to the southwesterly wind.

### 3.5. Forcing Mechanisms of Lake Circulation

We investigate here the role of wind curl, wind stress, and horizontal heterogeneities in the thermal structure as potential drivers of the lake circulation. As demonstrated in Section 3.3, the monthly mean depth-averaged circulation in LNC featured a predominant mid-lake cyclonic gyre throughout the ice-free season, a strong gyre or coastal currents in the eastern region during July–December, and strong northward currents along the western coast and fed into the mid-lake gyre during all months except in July–August. The prevailing southwesterly wind must be the main driving force for the coastal circulation, while the force mechanism for the mid-lake cyclonic gyre warrants further analysis. Previous studies have identified that in large stratified lakes both the wind stress and thermal structure (baroclinic effects) contribute to the formation of cyclonic gyre (Bennett, 1975; Beletsky et al., 2012; Csanady, 1977; Davidson et al., 1997; Schwab & Beletsky, 2003), and the thermally driven component is more steady while the wind-induced component is often transitory and tends to cancel out in the mean (Emery & Csanady, 1973; Schwab et al., 1995). We note that in stratified lakes, besides surface heat flux and mixing, the wind forcing can also affect the thermal structure. To explore the potential forcing mechanism we conducted three model sensitivity simulations by eliminating the wind stress curl (S1), surface heat flux (S2), or wind stress (S3) from the surface forcing fields, separately, and kept the other forcing components unchanged (Table 2).

Figures 13a and 13b show the monthly mean wind stress curl and the vorticity of the depth-averaged current in the central lake (30.62–30.82°N, 90.52–90.87°E) during May–December 2013. Figure 14 shows the monthly horizontal distributions of the depth-averaged water currents and water level during May, July, September, and November from cases S2 and S3.

Case S1 used the lake-averaged wind field with a zero curl. Compared with the original (base) run, the simulated mid-lake cyclonic gyre in S1 was slightly weakened, especially during August–December when the

**Table 2**

Configurations of the Sensitivity Experiments

Run	Surface momentum fluxes	Surface heat fluxes
S1	Spatially uniform winds	Yes
S2	Spatially variable winds	No
S3	No	Yes

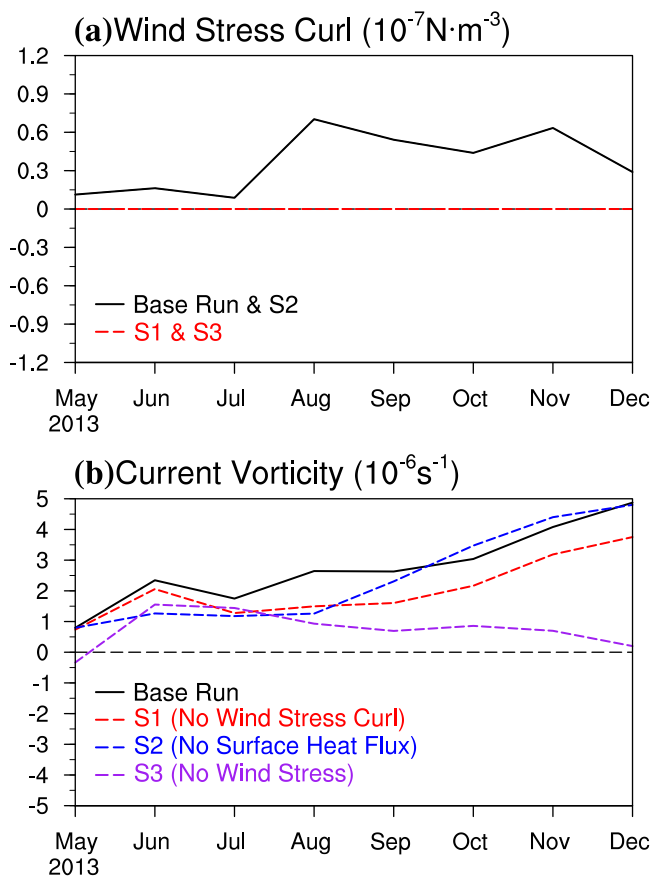


**Figure 13.** Monthly evolutions of (a) wind stress curl and (b) the vorticity of the depth-averaged current in the central lake ( $30.62\text{--}30.82^\circ\text{N}$ ,  $90.52\text{--}90.87^\circ\text{E}$ ) during May–December, 2013.

mid-lake wind stress curl showed large positive values (Figure 13). The thermal structure and large-scale circulation pattern modeled by S1 were overall very close to that in the base run (figures not shown), suggesting that the role of wind curl was not essential in driving the mid-lake cyclonic gyre. Case S2 contained purely wind-driven barotropic dynamics as the simulation started from the state of homogenous temperature with the surface heat flux set to zero. From Figure 14, the spatial distributions of water level and currents in S2 showed great resemblance with the base run, suggesting the dominance of wind in driving the circulation. During June–August when the lake was strongly stratified, the mid-lake gyre in S2 was weaker, and the vorticity of the mid-lake depth-averaged current showed smaller values (Figure 13). This suggested that the baroclinic effect was relatively more important for the mid-lake cyclonic gyre during stratified season. In case S3, the wind stress was set to zero hence it only included baroclinic dynamics driven by surface heat flux. From Figure 14, the depth-averaged lake circulation mainly showed a cyclonic gyre in the central lake. This gyre was relatively stronger during June–August when stratification was strong, but overall weaker than the base run and S1 and S2 with the presence of wind forcing. The coastal currents were nearly absent in S3, further confirming that the coastal circulation was mainly driven by wind.

#### 4. Summary

In this study, a 3-D lake model based on POM was for the first time applied to simulate the thermal structure and circulation during May–December 2013 in LNC, the third largest lake over TP. Simulation was also carried out using a previously developed 1-D model WRF-Lake. The solutions of the two models were compared with the horizontal structure of LST from the MODIS satellite remote sensing, and the vertical thermal structure from an in situ mooring located in the eastern part of the main basin. Results showed that LNC featured large thermal horizontal variability and the 3-D model was superior in modeling the thermodynamics

than the 1-D model. A heat budget analysis based on POM simulations further confirmed that besides the local lake-air heat flux, the lateral heat exchange also played a significant role in determining the spatiotemporal variability of the LST and vertical thermal structure in LNC.

Analyses of the simulation results of POM enabled the description of the evolution of the 3-D lake thermal structure and circulation during the ice-free period in LNC, which was characterized by springtime overturning, strong thermal stratification since summer, late autumnal overturning, and weak winter inverse thermal stratification. A typical “thermal bar” was formed in response to the density-driven convection induced by the radiative heating (surface cooling) during spring (autumn). Meanwhile, a predominant mid-lake cyclonic gyre existed throughout the ice-free period, and upwelling along the western coast and strong coastal currents occurred in all months except in July–August. Further model sensitivity experiments confirmed that the lake circulation primarily resulted from the wind-driven flow in response to the prevailing southwesterly wind, while the density-driven flow induced by the thermal process made a secondary contribution.

Several model deficiencies were identified and these need to be remedied for improved simulation of the thermo-hydrodynamics of LNC or other large alpine lakes over TP. One deficiency is that POM predicted a shallower mixed layer and a delayed destratification date at the LNC mooring site, indicating the underestimation of the vertical mixing strength due to missing the representation of mixing by, for example, Langmuir circulation and nonbreaking surface waves, and so on. Possible remedies are to implement the MY-2.5 turbulence closure scheme with a wind-wave-induced parameterization (Bai et al., 2013; Hu & Wang, 2010) or to couple the hydrodynamic model with a surface wave model, for example, WAVEWATCH



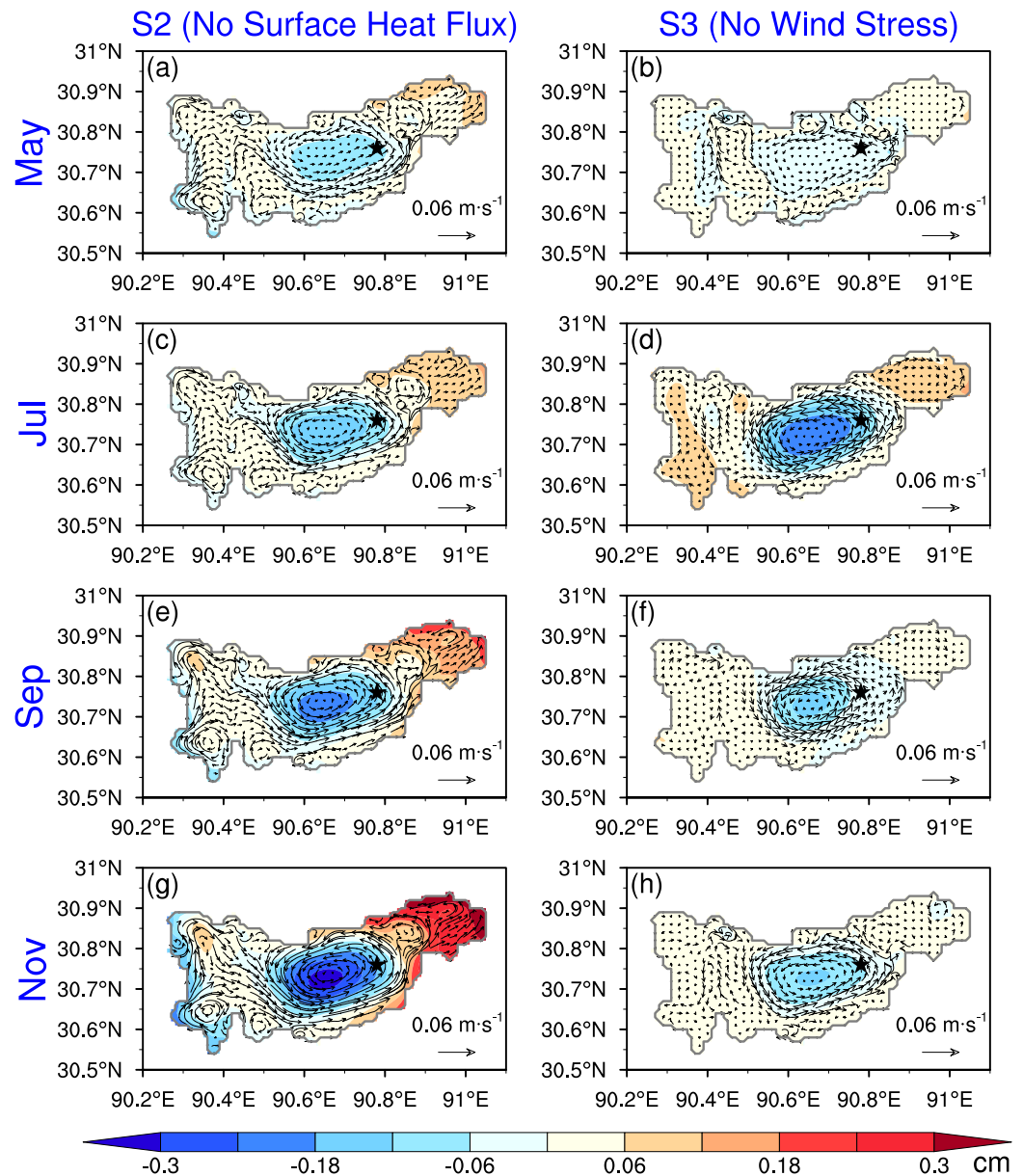


**Figure 14.** Monthly averaged lake water level (color shading) and depth-averaged currents (vectors) during May, July, September, and November in 2013 from the model run with no surface heat flux (S2, left column) and with no wind stress (S3, right column). The black solid asterisks represent the location of LNC mooring.

III (Tolman, 2009). Another deficiency is that the wind drag coefficient ( $C_d$ ) used in this study is a function of the near-surface wind speed without taking account of the influence of the atmospheric boundary stability. During fall when the atmospheric surface layer becomes unstable,  $C_d$  would be larger than the neutral value and this will lead to a more effective momentum transfer. In the present model the effect proposed by Emery and Csanady (1973), regarding the wind vorticity generated by the gradient of surface water temperature, may also be underrepresented. In addition, LNC and other high-altitude lakes in TP are usually covered by ice over an extensive period in a year, hence the mechanical and thermodynamic processes of ice also play important roles. Hence, it is necessary to incorporate an ice model component within the hydrodynamic models of these lakes. Finally, in view of the significant impact of wind fields on the accuracy of circulation and thermal structure, the quality of wind forcing needs to be assessed and improved with more comprehensive in situ wind observations, along with more observations of lake temperature and currents.

## Data Availability Statement

The authors are grateful to NASA for providing the MODIS LST product (MOD11; available at <https://modis.gsfc.nasa.gov/data/dataproduct/mod11.php>) and the Institute of Tibetan Plateau Research, Chinese Academy of Sciences (ITPCAS) for providing the China Meteorological Forcing Data Set (available at <https://data.tpdc.ac.cn/en/>).

## Acknowledgments

This study is supported by the National Natural Science Foundation of China under Grants 41975081, 41975130, the National Key R&D Program of China under Grant 2017YFA0604301, the Bilateral Research Project GZ1259 of the Sino-German Center for Research Support, CAS “Light of West China” Program (E12903010, Y929641001), the Jiangsu University “Blue Project” outstanding young teachers training object, the Fundamental Research Funds for the Central Universities and the Jiangsu Collaborative Innovation Center for Climate Change. The authors also appreciate Dr. Junbo Wang and Dr. Lei Huang for providing the station data, which is available at the National Tibetan Plateau Data Center. The authors thank the four anonymous reviewers for the very insightful, constructive, and detailed comments both on scientific analysis and presentation that guided the revision of the manuscript.

## References

- Aijaz, S., Ghantous, M., Babanin, A. V., Ginis, I., Thomas, B., & Wake, G. (2017). Nonbreaking wave-induced mixing in upper ocean during tropical cyclones using coupled hurricane-ocean-wave modeling. *Journal of Geophysical Research: Oceans*, *122*, 3939–3963. <https://doi.org/10.1002/2016jc012219>
- Bai, X. Z., Wang, J., Schwab, D. J., Yang, Y., Luo, L., Leshkevich, G. A., & Liu, S. Z. (2013). Modeling 1993–2008 climatology of seasonal general circulation and thermal structure in the Great Lakes using FVCOM. *Ocean Modelling*, *65*, 40–63. <https://doi.org/10.1016/j.oceanmod.2013.02.003>
- Beletsky, D., Hawley, N., & Rao, Y. R. (2013). Modeling summer circulation and thermal structure of Lake Erie. *Journal of Geophysical Research*, *118*, 6238–6252. <https://doi.org/10.1002/2013jc008854>
- Beletsky, D., Hawley, N., Rao, Y. R., Vanderploeg, H. A., Beletsky, R., Schwab, D. J., & Ruberg, S. A. (2012). Summer thermal structure and anticyclonic circulation of Lake Erie. *Geophysical Research Letters*, *39*, L06605. <https://doi.org/10.1029/2012gl015102>
- Beletsky, D., & Schwab, D. J. (2001). Modelling circulation and thermal structures in Lake Michigan: Annual cycle and interannual variability. *Journal of Geophysical Research*, *106*, 745–771. <https://doi.org/10.1029/2000jc000691>
- Beletsky, D., & Schwab, J. D. (2008). Climatological circulation in Lake Michigan. *Geophysical Research Letters*, *35*, L21604. <https://doi.org/10.1029/2008gl035773>
- Beletsky, D., Schwab, J. D., & McCormick, M. (2006). Modeling the 1998–2003 summer circulation and thermal structure in Lake Michigan. *Journal of Geophysical Research*, *111*, C10010. <https://doi.org/10.1029/2005jc003222>
- Bennett, J. R. (1975). Another explanation of the observed cyclonic circulation of large lakes. *Limnology & Oceanography*, *20*, 108–110. <https://doi.org/10.4319/lo.1975.20.1.0108>
- Bennington, V., Mckinley, G. A., Kimura, N., & Wu, C. H. (2010). General circulation of Lake Superior: Mean, variability, and trends from 1979 to 2006. *Journal of Geophysical Research*, *115*, C12015. <https://doi.org/10.1029/2010jc006261>
- Bennington, V., Notaro, M., & Holman, K. D. (2014). Improving climate sensitivity of deep lakes within a regional climate model and its impact on simulated climate. *Journal of Climate*, *27*, 2886–2911. <https://doi.org/10.1175/jcli-d-13-00110.1>
- Biermann, T., Babel, W., Ma, W. Q., Chen, X. L., Thiem, E., Ma, Y. M., & Foken, T. (2014). Turbulent flux observations and modelling over a shallow lake and a wet grassland in the Nam Co basin, Tibetan Plateau. *Theoretical and Applied Climatology*, *116*, 301–316. <https://doi.org/10.1007/s00704-013-0953-6>
- Blokhina, N. S., & Selin, D. I. (2019). Spring thermal bar formation in a water reservoir with a complex bottom relief (for Lake Ladoga as an example). *Moscow University Physics Bulletin*, *74*(1), 58–63. <https://doi.org/10.3103/s0027134919010065>
- Blumberg, A. F., & Mellor, G. L. (1987). A description of a three-dimensional coastal ocean circulation model, three-dimensional coastal ocean circulation model. In *Three-dimensional ocean models*. American Geophysical Union. <https://doi.org/10.1029/CO004p0001>
- Boyce, F. M., Donelan, M. A., Hamblin, P. F., Murthy, C. R., & Simons, T. L. (1989). Thermal structure and circulation in the great lakes. *Atmosphere-Ocean*, *27*(4), 607–642. <https://doi.org/10.1080/07055900.1989.9649358>
- Chen, Y. Y., Yang, K., He, J., Qin, J., Shi, J., Du, J., & He, Q. (2011). Improving land surface temperature modeling for dry land of China. *Journal of Geophysical Research*, *116*, D20104. <https://doi.org/10.1029/2011jd015921>
- Copernicus Climate Change Service (C3S). (2019). *C3S ERA5\_Land reanalysis*. Copernicus Climate Change Service. <https://doi.org/10.24381/cds.e2161bac>
- Craig, P. D., & Banner, M. L. (1994). Modeling wave-enhanced turbulence in the ocean surface layer. *Journal of Physical Oceanography*, *24*, 2546–2559. [https://doi.org/10.1175/1520-0485\(1994\)024<2546:mwvetit>2.0.co;2](https://doi.org/10.1175/1520-0485(1994)024<2546:mwvetit>2.0.co;2)
- Csanady, G. T. (1977). On the cyclonic mean circulation of large lakes. *Proceedings of the National Academy of Sciences of the United States of America*, *74*, 2204–2208. <https://doi.org/10.1073/pnas.74.6.2204>
- Dai, Y. F., Wang, L., Yao, T. D., Li, X. Y., Zhu, L. J., & Zhang, X. W. (2018). Observed and simulated lake effect precipitation over the Tibetan Plateau: An initial study at Nam Co Lake. *Journal of Geophysical Research: Atmospheres*, *123*, 6746–6759. <https://doi.org/10.1029/2018jd028330>
- Dai, Y. J., Wei, N., Huang, A. N., Zhu, S. G., Shang, G. W., Yuan, H., et al. (2018). The lake scheme of the common land model and its performance evaluation. *Chinese Science Bulletin*, *63*. <https://doi.org/10.1360/n972018-00609>
- Davidson, F. J. M., Greatbatch, R. J., & Goulding, A. D. (1997). On the net cyclonic circulation in large stratified lakes. *Journal of Physical Oceanography*, *25*, 1516–1520. [https://doi.org/10.1175/1520-0485\(1995\)025<1516:OTNCCI>2.0.CO;2](https://doi.org/10.1175/1520-0485(1995)025<1516:OTNCCI>2.0.CO;2)
- Emery, K. O., & Csanady, G. T. (1973). Surface circulation of lakes and nearly land-locked seas. *Proceedings of the National Academy of Sciences of the United States of America*, *70*, 93–97. <https://doi.org/10.1073/pnas.70.1.93>
- Garratt, J. R. (1977). Review of drag coefficients over oceans and continent. *Monthly Weather Review*, *105*(7), 915–929. [https://doi.org/10.1175/1520-0493\(1977\)105<0915:rodcoo>2.0.co;2](https://doi.org/10.1175/1520-0493(1977)105<0915:rodcoo>2.0.co;2)
- Gill, A. (1982). *Atmosphere-ocean dynamics*. Academic Press.
- Gou, P., Ye, Q. H., Che, T., Feng, Q., Ding, B. H., Lin, C. G., & Zong, J. B. (2017). Lake ice phenology of Nam Co, Central Tibetan Plateau, China, derived from multiple MODIS data products. *Journal of Great Lakes Research*, *43*, 989–998. <https://doi.org/10.1016/j.jglr.2017.08.011>
- Gu, H. P., Jin, J. M., Wu, Y. H., Ek, M. B., & Subin, Z. M. (2015). Calibration and validation of lake surface temperature simulations with the coupled WRF-lake model. *Climatic Change*, *129*, 471–483. <https://doi.org/10.1007/s10584-013-0978-y>
- Guo, Y. H., Zhang, Y. S., Ma, N., Xu, J. Q., & Zhang, T. (2019). Long-term changes in evaporation over Siling Co Lake on the Tibetan Plateau and its impact on recent rapid lake expansion. *Atmospheric Research*, *216*, 141–150. <https://doi.org/10.1016/j.atmosres.2018.10.006>
- He, J., Yang, K., Tang, W. J., Lu, H., Qin, J., Chen, Y. Y., & Li, X. (2020). Data descriptor: The first high-resolution meteorological forcing dataset for land process studies over China. *Scientific Data*, *7*(25), 1–11. <https://doi.org/10.1038/s41597-020-0369-y>

- Holland, P. R., & Kay, A. (2003). A review of the physics and ecological implications of the thermal bar circulation. *Limnologica*, 33, 153–162. [https://doi.org/10.1016/s0075-9511\(03\)80011-7](https://doi.org/10.1016/s0075-9511(03)80011-7)
- Hook, S. J., Prata, J., Alley, R. E., Abtahi, A., Richards, R. C., Schladow, S. G., & Palmansson, S. O. (2003). Retrieval of lake bulk and skin temperature using Along-Track Scanning Radiometer (ATSR-2) data: A case study using Lake Tahoe, California. *Journal of Atmospheric and Oceanic Technology*, 20(4), 534–548. [https://doi.org/10.1175/1520-0426\(2003\)20<534:rolbas>2.0.co;2](https://doi.org/10.1175/1520-0426(2003)20<534:rolbas>2.0.co;2)
- Hu, H. G., & Wang, J. (2010). Modeling effects of tidal and wave mixing on circulation and thermohaline structures in the Bering Sea: Process studies. *Journal of Geophysical Research*, 115, C01006. <https://doi.org/10.1029/2008jc005175>
- Huang, A. N., Lazhu, J. B., Wang, Y. J., Yang, K., Wei, N., et al. (2019). Evaluating and improving the performance of three 1-D Lake Models in a large deep lake of the Central Tibetan Plateau. *Journal of Geophysical Research*, 124, 3143–3167. <https://doi.org/10.1029/2018jd029610>
- Huang, A. N., Rao, Y. R., & Lu, Y. Y. (2010). Evaluation of a 3-D hydrodynamic model and atmospheric forecast forcing using observations in Lake Ontario. *Journal of Geophysical Research*, 115, C02004. <https://doi.org/10.1029/2009jc005601>
- Huang, C. J., & Qiao, F. L. (2010). Wave-turbulence interaction and its induced mixing in the upper ocean. *Journal of Geophysical Research*, 115, C04026. <https://doi.org/10.1029/2009jc005853>
- Huang, L., Wang, J. B., Zhu, L. P., Ju, J. T., & Daut, D. (2017). The warming of large lakes on the Tibetan Plateau: Evidence from a Lake Model Simulation of Nam Co, China, during 1979–2012. *Journal of Geophysical Research*, 122(13), 13,095–13,107. <https://doi.org/10.1002/2017jd027379>
- Hutter, K. (1984). *Hydrodynamics of lakes*. Springer-Verlag.
- Kantha, L. H., & Clayson, C. A. (2004). On the effect of surface gravity waves on mixing in the oceanic mixing layer. *Ocean Modelling*, 6(2), 101–124. [https://doi.org/10.1016/s1463-5003\(02\)00062-8](https://doi.org/10.1016/s1463-5003(02)00062-8)
- Ke, L. H., & Song, C. Q. (2014). Remotely sensed surface temperature variation of an inland saline lake over the central Qinghai-Tibet Plateau. *ISPRS Journal of Photogrammetry and Remote Sensing*, 98, 157–167. <https://doi.org/10.1016/j.isprsjprs.2014.09.007>
- Langmuir, I. (1938). Surface motion of water induced by wind. *Science*, 87, 119–123. <https://doi.org/10.1126/science.87.2250.119>
- Lazhu, K., Wang, J. B., Lei, Y. B., Chen, Y. Y., Zhu, L. P., et al. (2016). Quantifying evaporation and its decadal change for Lake Nam Co, central Tibetan Plateau. *Journal of Geophysical Research*, 121, 7578–7591
- Lu, S. L., Ma, J., Ma, X. Q., Tang, H. L., Zhao, H. L., & Baig, M. H. A. (2019). Time series of the inland surface water dataset in China (ISWDC) for 2000–2016 derived from MODIS archives. *Earth System Science Data*, 11, 1099–1108. <https://doi.org/10.5194/essd-11-1099-2019>
- Ma, R. H., Yang, G. H., Duan, H. T., Jiang, J. H., Wang, S. M., Feng, X. Z., et al. (2011). China's lakes at present: Number, area and spatial distribution. *Science China Earth Sciences*, 54, 283–289. <https://doi.org/10.1007/s11430-010-4052-6>
- Malm, J. (1995). Spring circulation associated with the thermal bar in large temperate lakes. *Hydrology Research*, 26, 331–358. <https://doi.org/10.2166/nh.1995.0019>
- Malm, J., Grahn, L., Mironov, D., & Terzhevik, A. (1993). Field investigation of the thermal bar in Lake Ladoga, spring 1991. *Hydrology Research*, 24, 339–358. <https://doi.org/10.2166/nh.1993.12>
- Martynov, A., Sushama, L., & Laprise, R. (2010). Simulation of temperature freezing lakes by one-dimensional lake models: Performance assessment for interactive coupling with regional climate models. *Boreal Environment Research*, 15, 143–164.
- Mellor, G. L. (1991). An equation of state for numerical models of oceans and estuaries. *Journal of Atmospheric and Oceanic Technology*, 8, 609–611. [https://doi.org/10.1175/1520-0426\(1991\)008<0609:aeofn>2.0.co;2](https://doi.org/10.1175/1520-0426(1991)008<0609:aeofn>2.0.co;2)
- Mellor, G. L., & Yamada, T. (1982). Development of a turbulence closure model for geophysical fluid problems. *Reviews of Geophysics*, 20(4), 851–875. <https://doi.org/10.1029/rg020i004p00851>
- Mortimer, C. H. (1987). Fifty years of physical investigations and related limnological studies on Lake Erie, 1928–1977. *Journal of Great Lakes Research*, 13, 407–435. [https://doi.org/10.1016/s0380-1330\(87\)71664-5](https://doi.org/10.1016/s0380-1330(87)71664-5)
- Mortimer, C. H. (2004). *Lake Michigan in motion: Response of an inland sea to weather, earth-spin, and human activities*.
- Murakami, T., Terai, H., Yoshiyama, Y., Tezuka, T., Zhu, L. P., Matsunaka, T., & Nishimura, M. (2007). The second investigation of Lake Puma Yum Co located in the Southern Tibetan Plateau, China. *Limnology*, 8, 331–335. <https://doi.org/10.1007/s10201-007-0208-2>
- Nyamweya, C., Desjardins, C., Sigurdsson, S., Tomasson, T., Taabu-munyaho, A., Sitoki, L., & Stefansson, G. (2016). Simulation of Lake Victoria circulation patterns using the Regional Ocean Modelling System (ROMS). *PLoS One*, 11(3), e0151272. <https://doi.org/10.1371/journal.pone.0151272>
- Rao, Y. R., & Schwab, D. J. (2007). Transport and mixing between the coastal and offshore waters in the Great Lakes: A review. *Journal of Great Lakes Research*, 33, 202–218. [https://doi.org/10.3394/0380-1330\(2007\)33\[202:tambtc\]2.0.co;2](https://doi.org/10.3394/0380-1330(2007)33[202:tambtc]2.0.co;2)
- Rao, Y. R., Skafel, M. G., & Charlton, M. N. (2004). Circulation and turbulent exchange characteristics during the thermal bar in Lake Ontario. *Limnology and Oceanography*, 49(6), 2190–2200. <https://doi.org/10.4319/lo.2004.49.6.2190>
- Schwab, D. J., & Beletsky, D. (2003). Relative effects of wind stress curl, topography, and stratification on large-scale circulation in Lake Michigan. *Journal of Geophysical Research*, 108, 3044. <https://doi.org/10.1029/2001jc001066>
- Schwab, D. J., O'Connor, W. P., & Mellor, G. L. (1995). On the net cyclonic circulation in large stratified lakes. *Journal of Physical Oceanography*, 25, 1516–1520. [https://doi.org/10.1175/1520-0485\(1995\)025<1516:otncci>2.0.co;2](https://doi.org/10.1175/1520-0485(1995)025<1516:otncci>2.0.co;2)
- Sharma, A., Hamlet, A. F., Fernando, H. J. S., Catlett, C. E., Horton, D. E., Kotamarthi, V. R., et al. (2018). The need for an integrated land-lake-atmosphere modeling system, exemplified by North America's Great Lakes Region. *Earth's Future*, 6, 1366–1379. <https://doi.org/10.1029/2018EF000870>
- Shepard, D. (1968). A two-dimensional interpolation function for irregularly-spaced data. In *Proceedings of the 1968 ACM National Conference, 27–29 August 1968, New York* (pp. 517–524). <https://doi.org/10.1145/800186.810616>
- Smagorinsky, J. (1963). General circulation experiments with the primitive equation. I. The basic experiment. *Monthly Weather Review*, 21, 99–164. [https://doi.org/10.1175/1520-0493\(1963\)091<0099:gcwptp>2.3.co;2](https://doi.org/10.1175/1520-0493(1963)091<0099:gcwptp>2.3.co;2)
- Song, C. Q., Huang, B., & Ke, L. H. (2014). Inter-annual changes of alpine inland lake water storage on the Tibetan Plateau, detection and analysis by integrating satellite altimetry and optical imagery. *Hydrological Processes*, 28(4), 2411–2418. <https://doi.org/10.1002/hyp.9798>
- Song, K. S., Wang, M., Du, J., Yuan, Y., Ma, J. H., & Mu, G. Y. (2016). Spatiotemporal variations of lake surface temperature across the Tibetan Plateau using MODIS LST product. *Remote Sensing*, 8, 854. <https://doi.org/10.3390/rs8100854>
- Song, Y., Semazzi, F. H. M., Xie, L., & Ogallo, L. J. (2004). A coupled regional climate model for the Lake Victoria basin of East Africa. *International Journal of Climatology*, 24, 57–75. <https://doi.org/10.1002/joc.983>
- Stepanenko, V., Jöhnk, K. D., Machulskaya, E., Perroud, M., Subin, Z., Nordbo, A., et al. (2014). Simulations of surface energy fluxes and stratification of a boreal lake by a set of one-dimensional models. *Tellus A: Dynamic Meteorology and Oceanography*, 66, 1. <https://doi.org/10.3402/tellusa.v66.21389>

- Subin, Z. M., Riley, W. J., & Mironov, D. (2012). An improved lake model for climate simulations: Model structure, evaluation, and sensitivity analyses in CESM1. *Journal of Advances in Modeling Earth Systems*, 4, M02001. <https://doi.org/10.1029/2011ms000072>
- Thikhomirov, A. I. (1963). The thermal bar of Lake Ladoga. *Bulletin (Izvestia) of the All-Union Geographical Society*, 95, 134–142.
- Titze, D. J., & Austin, J. A. (2014). Winter thermal structure of Lake Superior. *Limnology & Oceanography*, 59, 1336–1348. <https://doi.org/10.4319/lo.2014.59.4.1336>
- Tolman, H. L. (2009). *User manual and system documentation of WAVEWATCH III version 3.14*. Technical note, MMAB Contribution (Vol. 276).
- Tsydenov, B. O. (2019). A numerical study of the thermal bar in shallow water during the autumn cooling. *Journal of Great Lakes Research*, 45, 715–725. <https://doi.org/10.1016/j.jglr.2019.05.012>
- Verburg, P., & Antenucci, J. P. (2010). Persistent unstable atmospheric boundary layer enhances sensible and latent heat loss in a tropical great lake: Lake Tanganyika. *Journal of Geophysical Research*, 115, D11109. <https://doi.org/10.1029/2009jd012839>
- Wan, Z., Zhang, Y., Zhang, Q., & Li, Z. L. (2004). Quality assessment and validation of the MODIS global land surface temperature. *International Journal of Remote Sensing*, 25, 261–274. <https://doi.org/10.1080/0143116031000116417>
- Wang, J. B., Huang, L., Ju, J. T., Daut, D., Ma, Q. F., Zhu, L. P., et al. (2020). Seasonal stratification of a deep, high-altitude, Dimictic lake: Nam Co, Tibetan Plateau. *Journal of Hydrology*, 584, 124688. <https://doi.org/10.1016/j.jhydrol.2020.124688>
- Wang, J. B., Huang, L., Ju, J. T., Daut, D., Wang, Y., Ma, Q. F., et al. (2019). Spatial and temporal variations in water temperature in a high-altitude deep Dimictic mountain lake (Nam Co), central Tibetan Plateau. *Journal of Great Lakes Research*, 45, 212–223. <https://doi.org/10.1016/j.jglr.2018.12.005>
- Wang, J. B., Peng, P., Ma, Q. F., & Zhu, L. P. (2010). Modern limnological features of Tangra Yumco and Zhari Namco Tibetan Plateau. *Journal of Lake Sciences*, 22(4), 629–632.
- Wang, J. B., Zhu, L. P., Daut, G., Ju, J. T., Lin, X., Wang, Y., & Zhen, X. L. (2009). Investigation of bathymetry and water quality of Lake Nam Co, the largest lake on the central Tibetan Plateau. *Limnology*, 10, 149–158. <https://doi.org/10.1007/s10201-009-0266-8>
- Wang, M. D., Hou, J. Z., & Lei, Y. B. (2014). Classification of Tibetan lakes based on variations in seasonal lake water temperature. *Chinese Science Bulletin*, 59, 4847–4855. <https://doi.org/10.1007/s11434-014-0588-8>
- Wang, X. J., Pang, G. J., & Yang, M. H. (2017). Review Precipitation over the Tibetan during recent decades: A review based on observations and simulations. *International Journal of Climatology*, 38, 1116–1131. <https://doi.org/10.1002/joc.5246>
- Wen, L. J., Lv, S. H., Kirillin, G., Li, Z. G., & Zhao, L. (2016). Air–lake boundary layer and performance of a simple lake parameterization scheme over the Tibetan highlands. *Tellus A: Dynamic Meteorology and Oceanography*, 68(1), 31091. <https://doi.org/10.3402/tellusa.v68.31091>
- Wetzel, R. G., & Likens, G. E. (2000). The heat budget of lakes. In *Limnological analyses*. Springer. [https://doi.org/10.1007/978-1-4757-3250-4\\_4](https://doi.org/10.1007/978-1-4757-3250-4_4)
- Wu, Y., Huang, A., Lazhu, Yang, X., Qiu, B., Wen, L., et al. (2020). Improvements of the coupled WRF–Lake model over Lake Nam Co, Central Tibetan Plateau. *Climate Dynamics*, 55, 2703–2724. <https://doi.org/10.1007/s00382-020-05402-3>
- Wu, Y., Huang, A. N., Yang, B., Dong, G. T., Wen, L. J., Lazhu, et al. (2019). Numerical study on the climatic effect of the lake clusters over Tibetan Plateau in summer. *Climate Dynamics*, 53, 5125–5236. <https://doi.org/10.1007/s00382-019-04856-4>
- Xiao, C. L., Lofgren, B. M., Wang, J., & Chu, P. Y. (2016). Improving the lake scheme within a coupled WRF–lake model in the Laurentian Great Lakes. *Journal of Advances in Modeling Earth Systems*, 8, 1969–1985. <https://doi.org/10.1002/2016ms000717>
- Xiao, F., Ling, L., Du, Y., Feng, Q., Yan, Y., & Chen, H. (2013). Evaluation of spatial-temporal dynamics in surface water temperature of Qinghai Lake from 2001 to 2010 by using MODIS data. *Journal of Arid Land*, 5(4), 452–464. <https://doi.org/10.1007/s40333-013-0188-5>
- Xu, L. J., Liu, H. Z., Du, Q., & Wang, L. (2016). Evaluation of the WRF–lake model over a highland freshwater in southwest China. *Journal of Geophysical Research*, 121, 13989–14005. <https://doi.org/10.1002/2016jd025396>
- Xu, L. J., Liu, H. Z., Du, Q., Wang, L., Yang, L., & Sun, J. H. (2018). Differences of atmospheric boundary layer characteristics between pre-monsoon and monsoon period over the Erhai Lake. *Theoretical and Applied Climatology*, 135, 305–321. <https://doi.org/10.1007/s00704-018-2386-8>
- Xue, P. F., Pal, J. S., Ye, X. Y., Lenters, J. D., Huang, C. F., & Chu, P. Y. (2016). Improving the Simulation of Large Lakes in Regional Climate Modeling: Two-Way Lake–Atmosphere Coupling with a 3D Hydrodynamic Model of the Great Lakes. *Journal of Climate*, 1605–1627.
- Xue, P. F., Schwad, D. J., & Hu, S. (2015). An investigation of the thermal response to meteorological forcing in a hydrodynamic model of Lake Superior. *Journal of Geophysical Research: Oceans*, 120, 5233–5253. <https://doi.org/10.1002/2015jc010740>
- Zhang, G. Q. (2018). Changes in lakes on the Tibetan Plateau observed from satellite data and their responses to climate variations. *Progress in Geography*, 37(2), 214–223.
- Zhang, G. Q., Yao, T. D., Piao, S. L., Bolch, T., Xie, H. J., Chen, D. L., et al. (2017). Extensive and drastically different alpine lake changes on Asia's high plateaus during the past four decades. *Geophysical Research Letters*, 44, 252–260. <https://doi.org/10.1002/2016gl072033>
- Zhang, G. Q., Yao, T. D., Xie, H. J., Zhang, K. X., & Zhu, F. J. (2014). Lakes' state and abundance across the Tibetan Plateau. *Chinese Science Bulletin*, 59(24), 3010–3021. <https://doi.org/10.1007/s11434-014-0258-x>
- Zhang, Q. H., Jin, J. M., Zhu, L. J., & Lu, S. L. (2018). Modelling of water surface temperature of three lakes on the Tibetan Plateau using a physically based lake model. *Atmosphere–Ocean*, 56, 1–7. <https://doi.org/10.1080/07055900.2018.1474085>
- Zhu, L. J., Jin, J. M., Liu, X., Tian, L., & Zhang, Q. H. (2018). Simulations of the impact of lakes on local and regional climate over the Tibetan Plateau. *Atmosphere–Ocean*, 56(4), 230–239. <https://doi.org/10.1080/07055900.2017.1401524>